University of Glasgow
DEPARTMENT OF
AEROSPACE
ENGINEERING

Shock Reflection Hysteresis in an Underexpanded Jet : a CFD Study

B. J. Gribben, K. J. Badcock and B. E. Richards

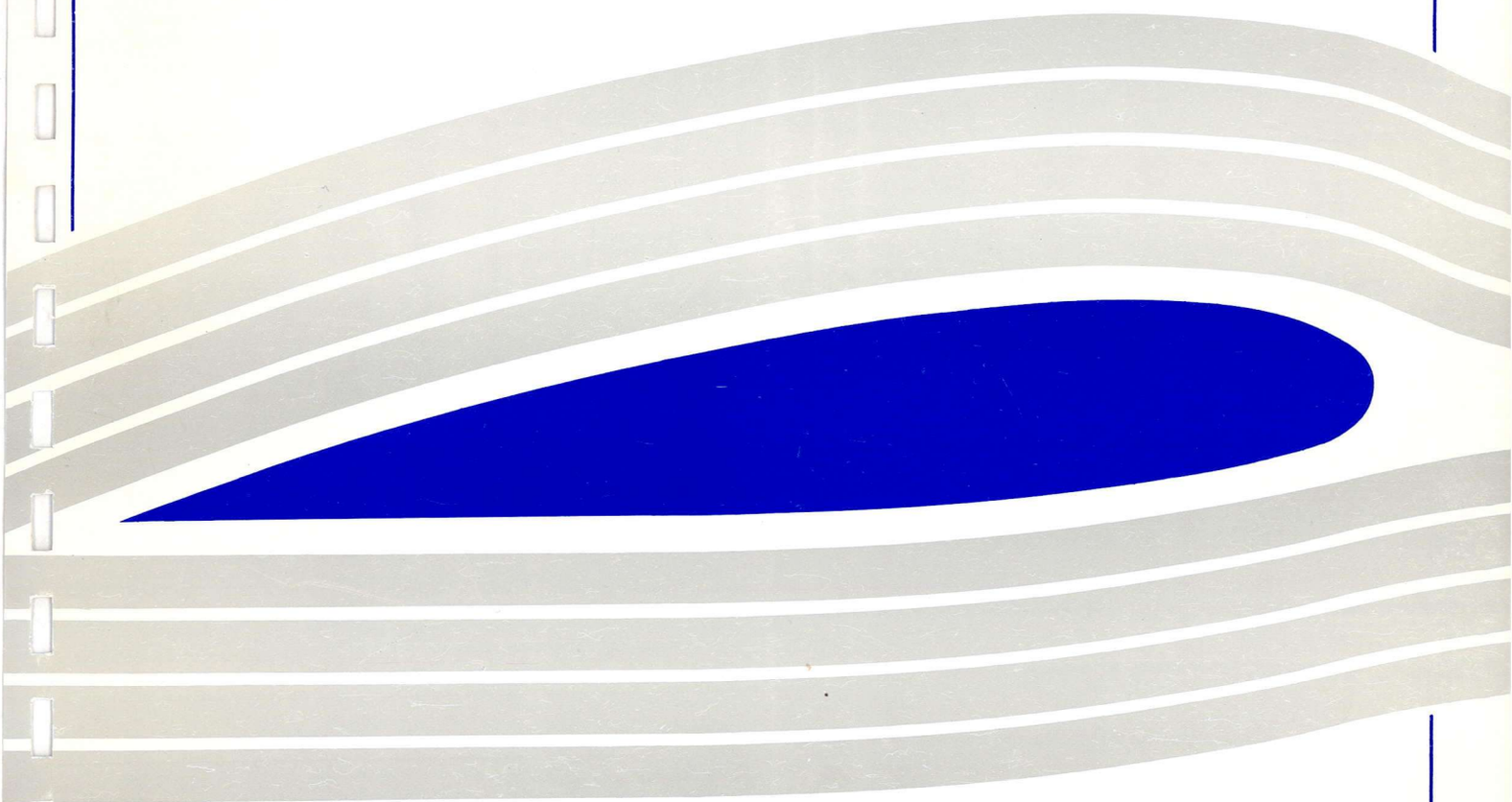

Shock Reflection Hysteresis in an Underexpanded Jet : a CFD Study

B. J. Gribben, K. J. Badcock and B. E. Richards

University of Glasgow

Department of Aerospace Engineering

Report Number 9808

April 1998

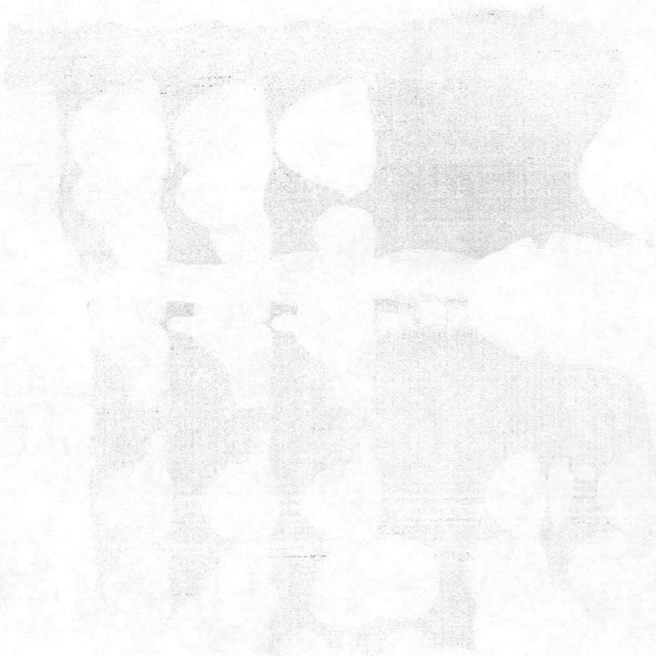

Abstract

Shock reflection hysteresis in a low density, axisymmetric underexpanded air jet is examined using a Navier-Stokes flow solver. Jets of this type are found in a number of applications e.g. rocket exhausts. The existence of a dual solution domain where either regular or Mach reflection may occur within the complex plume structure is predicted. This is in agreement with experiment where the same phenomenon has been observed for a nitrogen jet. The results of the computational study are used to examine the structure of the plume, and are compared with experimental data where available. The plume structure is complex, involving the interaction of several flow features, making this a demanding problem. A quasi-steady approach is employed in order to calculate the entire hysteresis loop. Included in this report is a review of the two dimensional shock reflection hysteresis problem. Some recommendations are made for further study of this type of flow.

Acknowledgements

Many thanks to Paul Welsh, Terry Cain and Martin Gilmore from Aerophysics, DERA Farnborough for introducing this problem and fruitful discussions during the course of the study. Thanks also to the other members of the CFD group within the Aerospace Engineering Department for their contributions, and Mark Allan for his initial work during the CFD Summer School.

This work is supported by a University of Glasgow scholarship and sponsorship from DERA Bedford.

Contents

List of Figures

Chapter 1

Introduction

1.1 Underexpanded Jets

A jet is said to be underexpanded if the gas pressure at the nozzle exit is greater than the ambient pressure. When this pressure ratio is large, the jet is said to be highly underexpanded and the jet plume is characterised by a complex repeated shock structure. Many examples of real aerodynamic flows where knowledge of the behaviour of this type of jet is necessary can be found in the literature. Rocket exhausts at high altitude may have highly underexpanded plumes. The study of such flows is important for predicting propulsive efficiency and plume signatures [1], [2],[3]. Experimental studies of these situations are also important for the validation of CFD codes which are used extensively in plume signature prediction work [2]. Vehicle manoeuvring thrusters may also give rise to underexpanded plumes [1], [2]. Proposed scramjet engine designs include supersonic underexpanded fuel injectors for which detailed modelling of the mixing process is required [4]. The behaviour of highly underexpanded jets must be understood for accurate consequence and risk assessment studies for accidental and operational releases of high pressure gas [5]. Underexpanded exhaust plumes interacting with the freestream may arise in aeropropulsion testing in wind tunnels [6]. An appreciation of underexpanded jet plume structures is important for the problems of plume-surface and plume-plume

interaction and avoiding wall interference when studying thruster nozzles in ground facilities like vacuum chambers [7]. Supersonic underexpanded jets are used in experiments to examine the aeroacoustic properties of strong shock cell structures [8]. Underexpanded hypersonic jets are used to study aerothermodynamic characteristics of hypersonic vehicle models in wind tunnels [9]. The same paper includes a very comprehensive account of how underexpanded jets are used in experimental and numerical studies of nonequilibrium thermo- and gasdynamic processes in hypersonic flow.

The experimental studies of Crist [1] and Abbett [10] established the basic wave structure of a highly underexpanded jet plume and that regular or Mach reflection may occur depending on the conditions. The method of characteristics has been employed by many authors [10], [11], [12], [13] in an attempt to develop predictive models for the core expansion and Mach disc location.

A phenomenon associated with low density highly underexpanded jets which has yet to be fully understood is shock reflection hysteresis as reported by Welsh [2]. For a (laminar) nitrogen jet exhausting from a nominally Mach 3 nozzle a set of conditions exist at which either regular or Mach reflection may occur depending on the history of the plume development. Since the reflection type strongly influences the interaction of the jet with its environment an understanding of the phenomenon and definition of the hysteresis loop limits are important. Quantitative experimental investigation of this problem, aside from being expensive, suffers from probe interference with the jet structure, necessitating the development of non-intrusive measurement techniques [2]. However, these promising methods have yet to reach full maturity and the potential of a CFD analysis is clear, providing the motivation for this study.

1.2 Shock Reflection Hysteresis

The existence of a hysteresis effect in the type of reflection of a two-dimensional oblique shock wave at a wall or symmetric line has been established in recent years. The reflection of the oblique shock wave may take the form of a regular reflection (RR) or Mach reflection (MR). The type of reflection which occurs depends on the Mach number upstream of the incident shock and the shock angle. However, there is a dual solution domain where either type may occur and the solution exhibits a hysteresis effect. A summary of the elements of this topic which are of interest to this study is included in Chapter 2.

1.3 CFD and Underexpanded Jets

Axisymmetric Euler and Navier-Stokes solvers have been used to obtain solutions for underexpanded jet plumes with impressive results, see for example [4], [5], [14], [15]. These calculations demonstrate good agreement with experiment for a wide range of conditions using parameters such as Mach disc location and centreline velocity and are reported to capture the complex wave structure in detail. No CFD study of the hysteresis phenomenon in underexpanded jets has been found. The hysteresis phenomenon associated with two-dimensional shock reflection has been successfully modelled numerically, see Chapter 2. In this case the crucial quantities (upstream Mach number and incident shock angle) are relatively easy to control and model correctly in a computational approach. However in the case of shock reflection in the underexpanded jet, these quantities are inherent parts of the calculation rather than being "set" a priori. All of the interacting features of the complex flow field must be resolved accurately, making this problem far more demanding. The application of a Navier-Stokes flow solver to shock reflection hysteresis in an underexpanded jet is described in Chapter 3, with the objective of contributing to the understanding of

this type of flow by combining the known features of two-dimensional shock reflection (see Chapter 2) with the detailed solutions provided by a CFD analysis.

Chapter 2

Two-Dimensional Shock Reflection Hysteresis

2.1 Introduction

Two different types of shock wave reflection, now known as Regular Reflection (RR) and Mach Reflection (MR), were first recorded by Ernst Mach in 1878. Analytic models for RR and MR were first developed by von Neumann in the 1940s. The existence of a hysteresis effect in the transition between types was first suggested in 1979 [16]. Subsequent experimental [17] and numerical studies [18],[19],[20] have since confirmed the existence of the phenomenon. These references together with review papers [21],[22] provide an extensive introduction to the topic of shock reflections and associated phenomena. This chapter summarises the parts of the above references relevant to the main study of underexpanded jets for which it is useful to introduce the theory and terminology of the two-dimensional case, and leans particulary on [17] and [21]. In addition, the current explanation for the hysteresis phenomenon is discussed. An attempt is made to fill the gaps in the explanation by applying the principle of minimum entropy production.

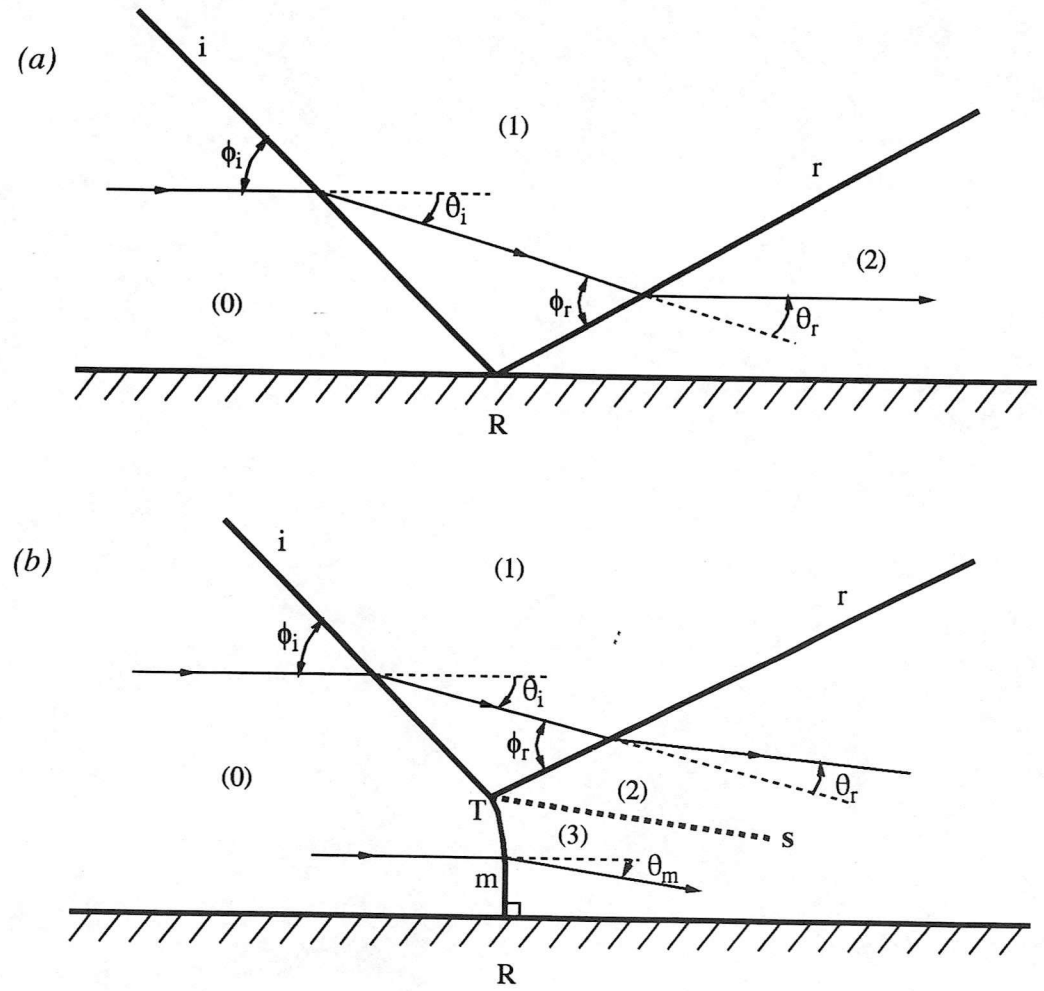

Figure 2.1: *Schematic diagrams of* (*a*) *regular reflection and* (*b*) *Mach reflection*

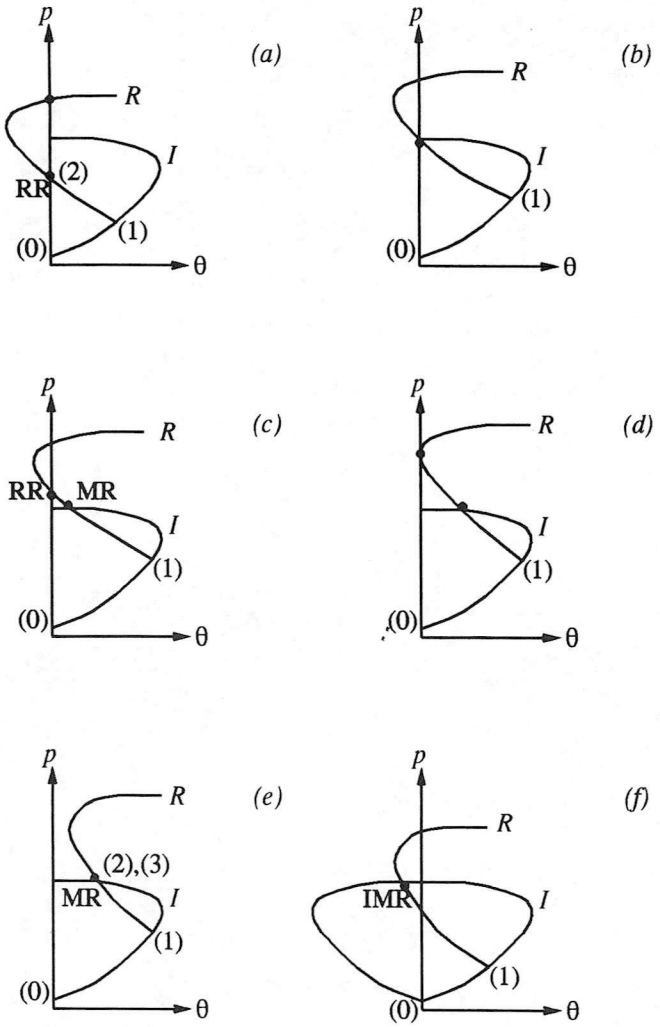

Figure 2.2: *Pressure-deflection diagrams*

2.2 Shock Reflection Types

Schematic diagrams of the Regular and Mach reflection types are shown in Figure 2.1. In the figures, **i** is the incident shock wave, **r** is the reflected shock wave, **m** is the Mach stem and **s** is the slip line. The reflection and triple points are labelled **R** and **T** respectively. ϕ_i and ϕ_r are the incidence angles of **i** and **r** respectively. θ_i, θ_r and θ_m are the flow deflections on passing through **i**, **r** and **m** respectively. The regular reflection, as shown in Figure 2.1(a), consists of an incident and reflected shock wave meeting at point **R** on the reflecting surface. The incidence angle ϕ_i is small enough such that the flow deflection caused by the reflected shock wave is sufficient to cancel that caused by the incident shock wave. In this way the condition of flow tangency at the reflecting surface is maintained. Thus the boundary condition for RR is

$$\theta_i - \theta_r = 0 \tag{2.1}$$

The Mach reflection type, shown in Figure 2.1(b), consists of incident and reflected shock waves, a Mach stem and a slip line, all of which meet at the triple point. The Mach stem is perpendicular to the reflecting surface and may curve as shown to become concave as viewed from upstream. The flow being processed by the Mach stem may be considered to form a buffer region between the flow tangency condition at the reflecting surface and a detached regular reflection which cannot maintain this condition on its own. The flow behind the Mach stem is subsonic. The net flow deflection behind the triple point is in general non-zero. Note that since the Mach stem is curved the conditions in region (3) are non-uniform; conditions behind the Mach stem in the vicinities of **R** and **T** will be denoted with the subscripts $_{3,R}$ and $_{3,T}$ respectively. Since flow on either side of the slip line must be parallel, the boundary conditions for a Mach reflection are

$$\begin{aligned} \theta_i - \theta_r &= \theta_m \\ p_2 &= p_{3,T} \end{aligned} \tag{2.2}$$

It is important to note that equation (2.1) considers local conditions in the vicinity of **R** only. In the same way equations (2.2) consider local conditions in the vicinity of **T**. To apply these relations globally the shock waves **i** and **r** and slip line **s** must be straight, implying regions of uniform flow.

2.3 The Dual Solution Domain

Graphical solutions in the pressure-deflection ($p-\theta$) plane, which are obtained from oblique shock theory [23], are useful for understanding shock-wave phenomena, and in particular the conditions for which each reflection type is possible. Figures 2.2 are examples of ($p-\theta$) diagrams. In these figures, the I polar represents the locus of all possible solutions (1) when the free-stream state (0) is deflected through an angle θ via an oblique shock wave. Similarly, the R polar represents the locus of all possible solutions (2) when the free-stream (1) is deflected through an angle θ via an oblique shock wave. In the figures θ_i is increasing as we progress from Figure 2.2(a) to Figure 2.2(e). The RR boundary condition (2.1) implies that the solution of a regular reflection is at a point where the R polar intersects the p-axis, i.e. where θ is zero. Figure 2.2(a) shows two such points; the higher pressure point is observed to be unstable in experiments [17] and has been shown to be aphysical [24], a result which will be discussed in Section 2.6.2. Consequently, conditions at (2) are represented by the point RR. The MR boundary conditions (2.2) imply that the solution of a Mach reflection is at a point where the I and R polars intersect, e.g. Figure 2.2(e). States (2) and (3) of Figure 2.1(b) map onto the point MR indicated, state (2) being on R and state (3) on the I polar.

Three interesting cases which lie between those discussed above are shown in Figures 2.2(b) to 2.2(d). First, reconsider the case represented by Figure 2.2(a). If the

upstream Mach number is held constant but the angle ϕ_i is gradually increased then the solution point RR moves up the p-axis until the condition represented by Figure 2.2(b) is reached. Since at this point both polars and the p-axis intersect, both RR and MR solutions are possible. The smallest incident shock angle for which MR is possible for a given upstream Mach number is represented at this point (except in the special case of *Inverted* Mach Reflection as discussed below). This condition is known as the *von Neumann criterion.* As ϕ_i is increased further the situation represented by Figure 2.2(c) occurs. The R polar intersects both the I-polar and the p-axis, so again both RR and MR solutions are possible although in this case with different values of p and θ. This figure represents typical solutions in the dual solution domain. The second limit of the dual solution domain is represented by Figure 2.2(d) where ϕ_i has been further increased such that the R-polar is tangent to the p-axis. The largest incident shock angle for which RR is possible for a given upstream Mach number is represented at this point. This condition is known as the *detachment criterion.* Any further increase in ϕ_i results in the situation shown in Figure 2.2(e) where the R-polar no longer intersects the p-axis so only MR is now possible.

As noted above, the von Neumann condition is at present accepted as the lower pressure limit to the dual solution domain. Recall that this condition is represented in the (p, θ) plane by Figure 2.2(b). If from this condition the incident shock angle is increased then RR is observed, see Figure 2.2(a). Hornung[21] discusses the alternative of *Inverted* Mach Reflection (IMR): if we consider that the flow may be deflected away from the wall by MR, i.e. θ_w in Figure 2.1(b) is negative, then this would be represented in the (p, θ) plane by the point IMR in Figure 2.2(f). The curvature of $\mathbf{m}$ is then necessarily convex as seen from upstream in order to achieve this deflection. Note that an IMR always has the alternative of a RR. The reflection

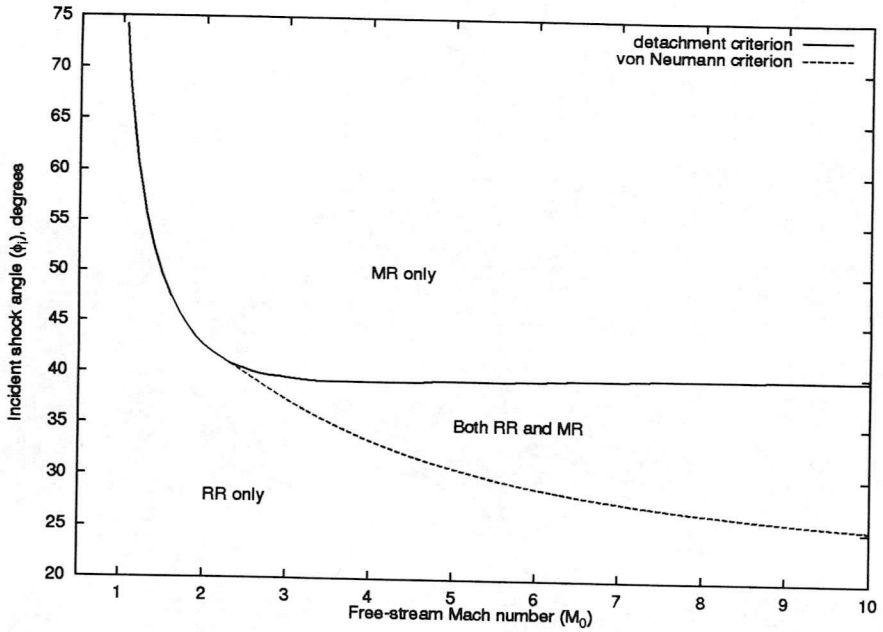

Figure 2.3: *Domains of possible reflection types*

type observed in experiment is RR unless it is suppressed by raising the downstream pressure, in which case the IMR occurs [21],[25]. This phenomenon has yet to be fully explained, and will be returned to in Section 2.6.3.

2.4 Analytic Solutions in the Dual Solution Domain

Analytic solutions for RR, MR the von Neumann and detachment criteria will be used in this study. They are readily obtained using the arguments of Section 2.3 and oblique shock theory, making certain simplifying assumptions for the MR calculations. Their calculation is straightforward and is outlined here for completeness. Figure 2.3 indicates the location of the dual solution domain in the (M_0,ϕ_i) plane. The overlap region where both RR and MR are possible is clearly shown.

2.4.1 Oblique Shocks

A result of oblique shock wave theory (see for example [26]) is that for any given upstream Mach number M_0 the same flow deflection θ can be achieved via two distinct straight shock solutions, provided that θ is less than the maximum deflection possible θ_{max}. This result is demonstrated in Figure 2.4 where the curve is the locus of all possible solutions in the (θ,β) plane when a free-stream of Mach number M_0 is deflected through an angle θ by an oblique shock wave at angle β to the free-stream. The solution corresponding to the larger value of β is termed the 'strong' solution since the changes across the shock are more severe than for the 'weak' solution at the shallower angle. The density, pressure, Mach number and temperature changes across an oblique shock are given by

$$\frac{\rho_1}{\rho_0} = \frac{(\gamma+1)\,M_0^2 \sin^2\beta}{(\gamma-1)\,M_0^2 \sin^2\beta + 2} \tag{2.3}$$

$$\frac{p_1}{p_0} = 1 + \frac{2\gamma}{\gamma+1}\left(M_0^2 \sin^2\beta - 1\right) \tag{2.4}$$

$$M_1^2 \sin^2(\beta-\theta) = \frac{M_0^2 \sin^2\beta + [2/(\gamma-1)]}{[2\gamma/(\gamma-1)]\,M_0^2 \sin^2\beta - 1} \tag{2.5}$$

$$\frac{T_1}{T_0} = \frac{p_1}{p_0}\frac{\rho_0}{\rho_1} \tag{2.6}$$

where (0) and (1) denote conditions before and after the shock respectively and γ is the ratio of specific heats. The flow deflection θ due to the oblique shock is given by

$$\tan\theta = 2\cot\beta\left[\frac{M_0^2 \sin^2\beta - 1}{M_0^2(\gamma + \cos 2\beta) + 2}\right] \tag{2.7}$$

Thus given the upstream conditions and shock angle β the downstream conditions can be calculated in a very straightforward manner.

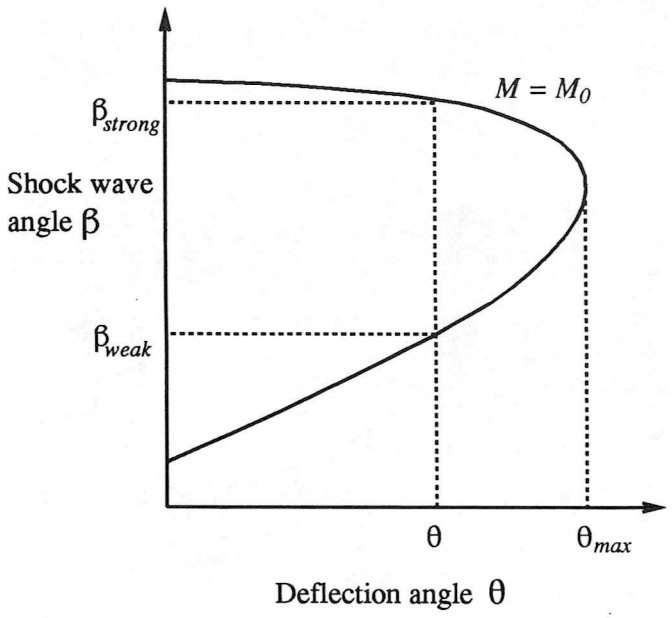

Figure 2.4: *Weak and strong solutions in the (θ,β) plane*

2.4.2 Regular Reflection

A regular reflection solution involves two oblique shocks. Referring to Figure 2.1(a), the conditions at (1) and the deflection θ_i are calculated using the oblique shock relations, see directly above. To calculate the conditions at (2), ϕ_r is obtained by invoking the condition (2.1) and solving equation (2.7). It is not possible to solve for ϕ_r directly so a simple iterative procedure (such as a bisection method) is required. Note that the 'weak' solution can normally assumed to be correct in the absence of additional boundary conditions (see Section 2.6.2). Figure 2.5 includes the pressure ratio $p_{2,RR}/p_0$ for various M_0 within the dual solution domain, the subscript RR referring to the regular reflection type discussed here. Note that in the figure each curve extends from $\phi_i = \phi_i^N$ on the left of each curve to $\phi_i = \phi_i^D$ on the right.

2.4.3 The Detachment Criterion

For a given free-stream Mach number M_0 the incident shock angle ϕ_i^D corresponding to the detachment criterion (see Section 2.3) is obtained by gradually increasing ϕ_i

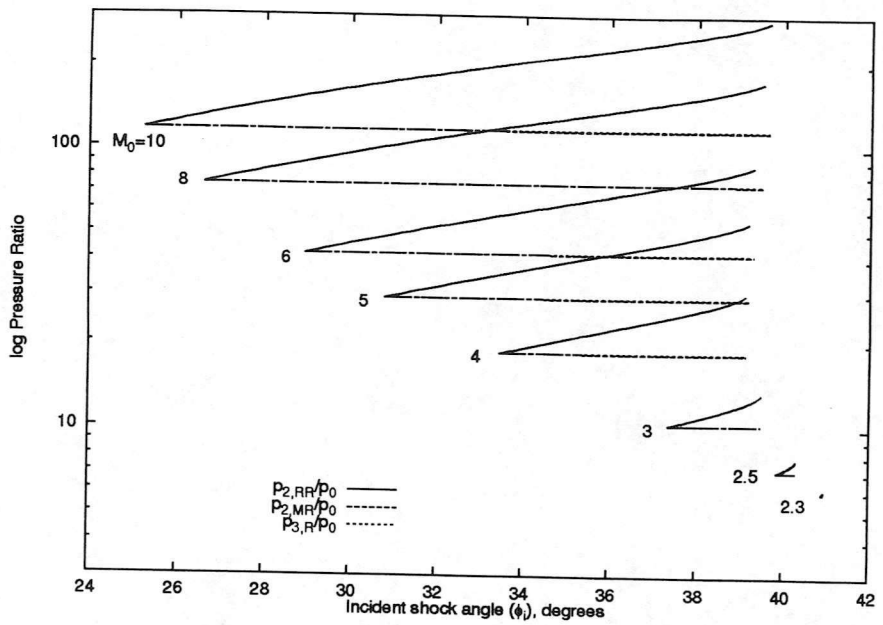

Figure 2.5: *Pressure ratios across shock reflections in dual solution domain*

when calculating a RR until the solution for **r** can no longer be achieved. The variation of ϕ_i^D with M_0 is shown in Figure 2.3.

2.4.4 The von Neumann Criterion

For a given free-stream Mach number M_0 the incident shock angle ϕ_i^N corresponding to the von Neumann criterion (see Section 2.3) is obtained by first calculating the pressure $p_{3,R}$ behind a normal shock. For some small value of ϕ_i a RR solution is then calculated; the pressure p_2 behind **r** should be less than $p_{3,R}$. ϕ_i is then gradually increased until p_2 equals $p_{3,R}$. The variation of ϕ_i^N with M_0 is shown in Figure 2.3. Note that for $M_0 \leq 2.20$ the von Neumann criterion does not exist.

2.4.5 Mach Reflection

Referring to Figure 2.1(b), a first guess for the conditions at (2) and (3,T), for which the boundary conditions (2.2) apply, is obtained by calculating the pressure behind **T** if **m** is locally normal to the flow, i.e. by taking $p_{3,R}$ as an initial guess for $p_{3,T}$. The deflections θ_m and θ_r are then calculated for this pressure value using

equation (2.7) with equation (2.4), the conditions at (0) and (1) being known. The pressure $p_{3,T}$ is gradually decreased until the conditions (2.2) are true. Note that this analysis gives a 'Mach reflection solution' in that the gasdynamic conditions at (0),(1),(2) and (3) are known. However, note that the length of **m** and its inclination between **R** and **T** are not calculated. A more involved approach has been used[27] to estimate the length of **m** with some success. Regarding the conditions in region (3), note that this analysis yields two sets of conditions here; conditions (3,T) behind **T** which uphold the MR boundary conditions, and conditions (3,R) behind **R** where **m** is normal to the free-stream. Figure 2.5 includes the pressure ratios $p_{2,MR}/p_0$ and p_3/p_0 for various M_0 within the dual solution domain. Note that $p_{2,MR}/p_0$ and $p_{3,T}/p_0$ are equivalent due to condition (2.2). Note also that $p_{2,MR}/p_0$ and $p_{3,R}/p_0$ diverge by only a very small amount; in Figure 2.5 their respective curves are all but identical.

2.5 The Hysteresis Phenomenon

Pressure-deflection maps provide useful illustrations of how a dual solution domain can occur. However, when more than one reflection type is possible no clue is given by these maps as to which mode actually occurs. The existence of a hysteresis effect in the shock reflection type in the dual solution domain was first postulated by Hornung[16]. A number of relatively recent experimental studies have contributed to the understanding of this type of flow [16],[23],[25],[28] culminating in the first experimentally recorded shock reflection hysteresis [17]. Figure 2.6 shows schematically a typical experimental set up for examination of this problem. Wave diagrams for (a) Regular Reflection and (b) Mach Reflection are also shown. Recent numerical studies have also predicted the phenomenon [18],[19],[20],[29]. If the dual solution domain is approached from a condition for which only RR may occur, then RR persists until the detachment criterion is reached where the reflection type flips to

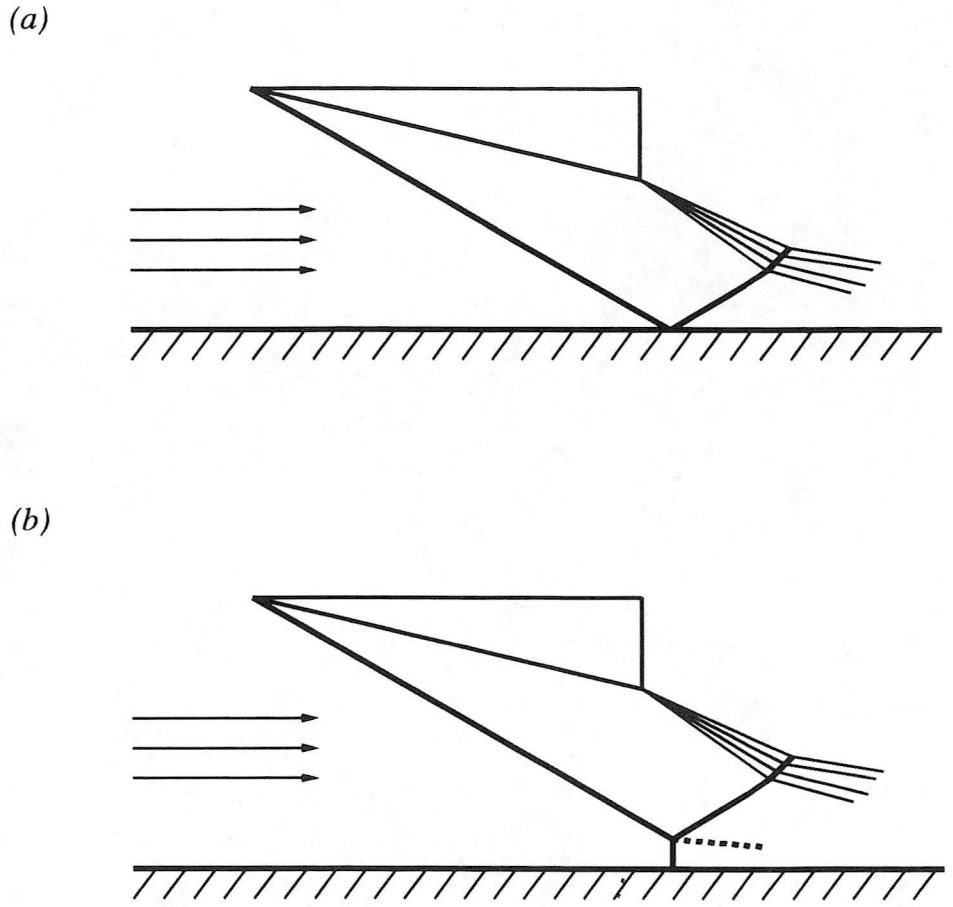

Figure 2.6: *Use of a wedge shock generator for (a) regular reflection and (b) Mach reflection experiments*

MR. Likewise, if the dual solution domain is approached from a MR condition, then MR persists until the von Neumann condition is reached where the reflection type flips to RR. Figure 2.7 shows a schematic representation in the $(\phi_i, l_m/w)$ plane, l_m being the length of the Mach stem **m**, and w being the length of the wedge from leading to trailig edge. Note that as the von Neumann condition is approached, l_m becomes vanishingly small. The most complete explanation to date for the hysteresis is provided by Hornung [21] and is summarised below.

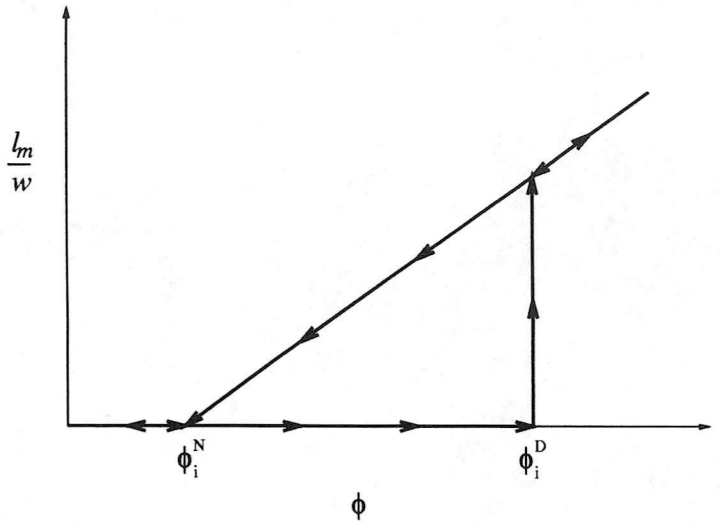

Figure 2.7: *Schematic illustration of the hysteresis loop in the (ϕ_i,l_m) plane*

A feature of MR not present in RR is the existence of a characteristic length, namely the length of the Mach stem. In the absence of mechanisms which may provide a characteristic length scale such as viscous effects, heat dissipation and relaxation, the length scale must be provided by the geometry of the boundary conditions. The obvious candidate is the length w from the leading to trailing edge of the wedge creating the incident shock. Such a wedge has been used in all experiments to date. The *information condition* requires that for MR to occur an information path must be open from the trailing edge of the wedge to the interaction area in order to transmit the characteristic length information. This information path is provided by an expansion from the trailing edge reaching the subsonic area behind the Mach stem. The transition criteria are then explained using this condition. An information path does not exist in the case of RR, thus when the dual solution domain is approached from a RR condition, the RR persists until the detachment criterion is reached. An information path is open in the case of MR, thus when the dual solution domain is approached from a MR condition, there is no impediment to MR occurring so it

persists until the von Neumann criterion is reached.

This description of the mechanisms causing the hysteresis does not seem complete. The explanation for the persistence of RR until the detachment condition is reasonable. However, for the persistence of MR, it has only been explained how there is no impediment to MR; it has not been explained why the MR should persist in preference to RR. An explanation for the MR persistence symmetrical to the RR persistence argument would require an identified impediment to the existence of RR when an MR condition exists within the dual solution domain. An alternative approach is the possibility that when either RR or MR is possible, MR may be the preferred solution. Note that such an argument would not contradict the above explanation for the persistence of RR (where MR is impeded). An explanation of why MR is preferred would then constitute an explanation for the persistence of MR, i.e. for one half of the hysteresis loop. The principle of minimum entropy production will be applied to this problem in Section 2.6.4 in an attempt to contribute to the explanation of the hysteresis phenomenon.

2.6 The Principle of Minimum Entropy Production

The principle of minimum entropy production [30] states that if more than one steady state solution is compatible with the problem boundary conditions then nature prefers the solution of minimum dissipative structure i.e. the observed solution is that with the minimum rate of entropy production. The principle has been applied to the deflection of supersonic flow by wedges to explain the prevalence of 'weak' over 'strong' shock solutions [24],[31]. By extension, the prevalence of 'weak' over 'strong' regular reflections, a problem already mentioned in Section 2.3, has also

been explained using this principle [24]. Pseudo-steady shock reflection (as opposed to the steady shock reflections considered in this work) have also been examined using the principle [32]. Thus a precedent clearly exists for using the principle to help explain phenomena associated with shock wave reflections. Encouraged by this, the principle will be applied below to two shock reflection phenomena which in the authors' opinion have not yet been fully explained, namely why the von Neumann criterion is the lower pressure limit on the dual solution domain and IMR is not normally observed (see Section 2.3) and the persistence of MR in the hysteresis loop (see Section 2.5). As a preliminary, the principle is first re-applied to supersonic flow deflection and regular shock reflections.

2.6.1 Supersonic Flow Deflection

If a supersonic free-stream of Mach number M_0 is deflected by a wedge at incidence θ to the free-stream (θ being less than the shock detachment angle) then oblique shock theory admits two solutions (see Section 2.4.1). For an ideal gas [33]

$$ds = C_p \, d\ln T - R \, d\ln p \tag{2.8}$$

which can be integrated directly to yield

$$s_1 - s_0 = C_p \, d\ln \frac{T_1}{T_0} - R \, d\ln \frac{p_1}{p_0} \tag{2.9}$$

which is an expression for the increase in entropy when an ideal gas is changed from state (0) to state (1) by some process. Here C_p is the specific heat at constant pressure and R is the specific gas constant. If the process is an oblique shock, then equations (2.3) to (2.6) can be substituted into equation (2.9) to obtain

$$\begin{aligned} s_1 - s_0 = C_v \Bigg\{ & \gamma \ln \left[\frac{2}{(\gamma+1) M_0^2 \sin^2\beta} + \frac{\gamma-1}{\gamma+1} \right] \\ & + \ln \left[\frac{2\gamma}{\gamma+1} M_0^2 \sin^2\beta - \frac{\gamma-1}{\gamma+1} \right] \Bigg\} \end{aligned} \tag{2.10}$$

where C_v is the specific heat at constant volume. Figure 2.8 shows the entropy increase across an oblique shock calculated using this expression for various free-stream Mach numbers M_0 with air as the working gas. It is evident that the entropy increase across the shock increases with shock angle, as might be expected. The 'strong' oblique shock solution has a greater shock angle than the 'weak' solution, and hence has a greater associated entropy rise. This can be stated as

$$\Delta s_{strong} > \Delta s_{weak} \tag{2.11}$$

If J is the shape of the reflected shock wave front then the rate of entropy production $\dot{S}$ across the shock is given by [24]

$$\dot{S} = \int_J \rho_0 u_0 \sin\beta(s_1 - s_0)dw \tag{2.12}$$

where dw is a differential line element along J. In this case the shock wave is straight and the entropy increase across the shock does not change along J. Since the total mass flow rate must remain constant (the upstream conditions (0) are not influenced by the reflected shock angle) an increasing entropy jump across the shock implies increasing entropy production. Thus condition (2.11) implies

$$\dot{S}_{strong} > \dot{S}_{weak} \tag{2.13}$$

and by the principle of minimum entropy production the 'weak' solution is the stable i.e. physical solution.

As noted in Salas[31] the principle of minimum entropy production explains the prevalence of 'weak' over 'strong' oblique shock solutions in the simple deflection of supersonic flow, but does not disprove the possibility of a 'strong' shock solution if the downstream pressure is given as a boundary condition. The principle of minimum entropy production applies only when multiple steady states occur which satisfy the same boundary conditions. Thus in this case for a fixed M_0 and θ from

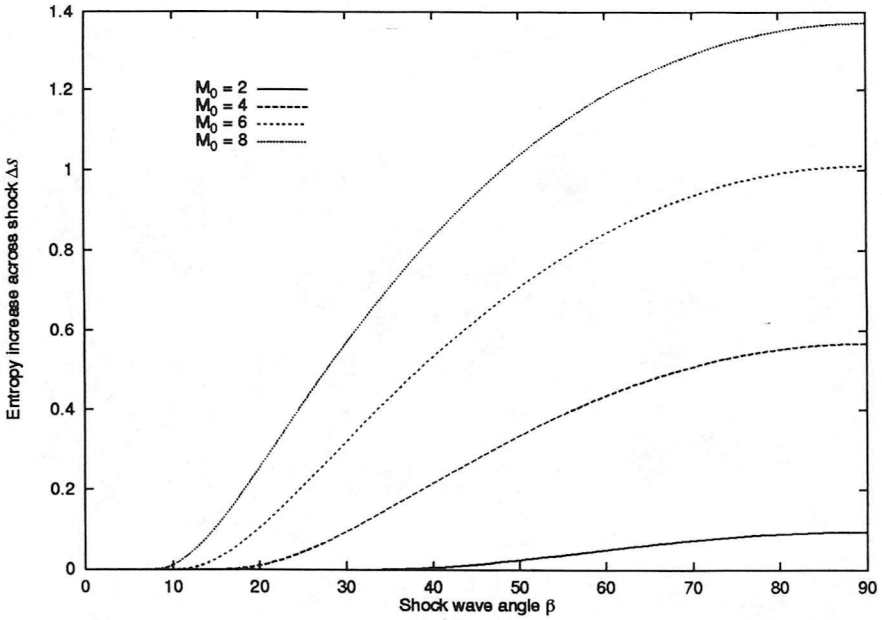

Figure 2.8: *Increase in entropy across an oblique shock*

oblique shock theory both β_{strong} and β_{weak} could occur but the principle indicates β_{weak}. However if the downstream pressure is given as a boundary condition then the boundary condition set has changed and the only possible solution is some θ which satisfies the pressure.

2.6.2 Regular Reflection

As has been mentioned in Section 2.3, two possible RR solutions exist when $\phi_i < \phi_i^D$. This situation is represented in the (p, θ) plane in Figure 2.2(a). The two possible solutions, at the points where the R polar intersects the p axis, arise because two values of reflected shock angle $\phi_{r,weak}$ and $\phi_{r,strong}$ can achieve the θ_r necessary to satisfy the RR boundary condition (2.1). This situation is clearly very similar to supersonic flow deflection (see directly above) and the result is the same; the principle of minimum entropy production predicts that for a given M_0 and ϕ_i the 'weak' solution is observed since it entails a lower rate of entropy production. The entropy increase $\Delta s = s_2 - s_0$ variation with ϕ_i for various M_0 across an RR with

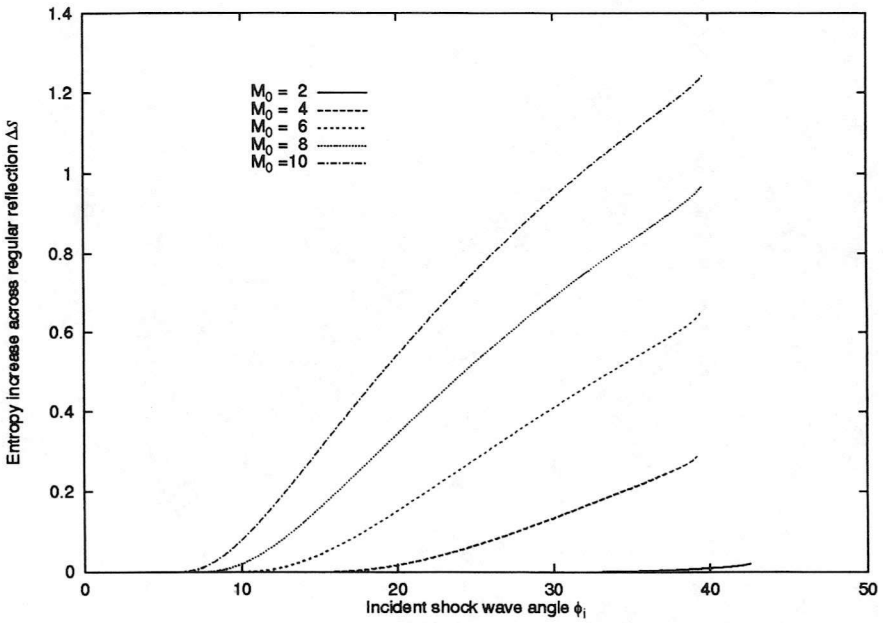

Figure 2.9: *Increase in entropy across a regular reflection*

a 'weak' reflected shock is shown in Figure 2.9. That the entropy increase in each case would be greater for a 'strong' solution is evident from Figure 2.8 if ϕ_r and M_1 are substituted for β and M_0. Note that the posssibility of a 'strong' RR has not been disproved, see the end of Section 2.6.1.

2.6.3 Inverted Mach Reflection

As has been discussed in Section 2.3, why the von Neumann condition should mark the lower pressure end of the dual solution domain and IMR is not normally observed has yet to be fully explained. In this and in subsequent sections the conditions in region (3) behind **R** will be denoted with the subscript $_3$ rather than with $_{3,R}$ to shorten the notation. Note that the conditions in region (3) behind **T** are equivalent to those in region (2) behind **r** in the cae of MR so the subscript notation $_{3,T}$ is now discarded. Figures 2.10 and 2.11 show the calculated entropy increases across a regular reflection ($s_{2,RR} - s_0$) and the oblique ($s_{2,MR} - s_0$) and Mach stem ($s_3 - s_0$) parts of a Mach reflection within the dual solution domain for a representative range

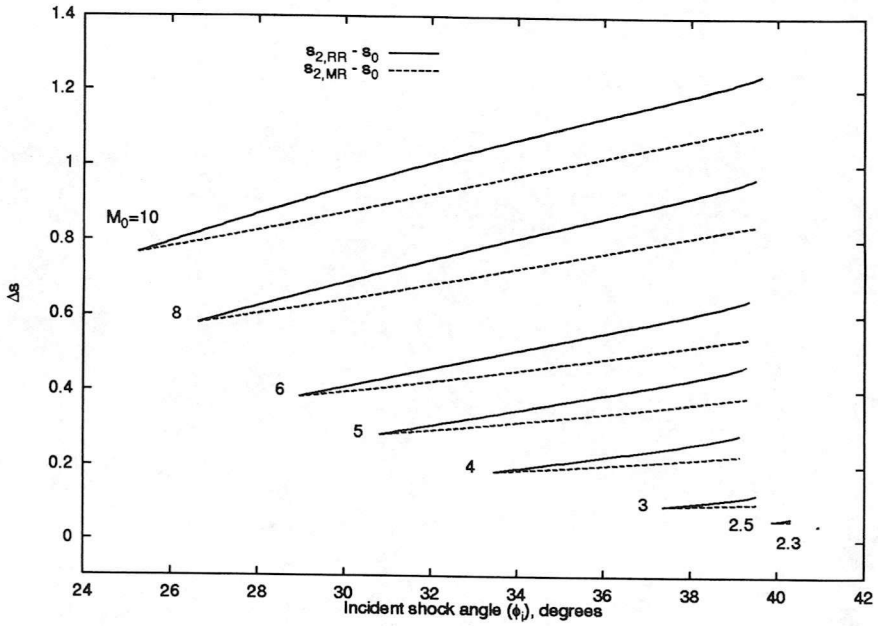

Figure 2.10: *Entropy increase across RR and oblique part of MR in dual solution domain*

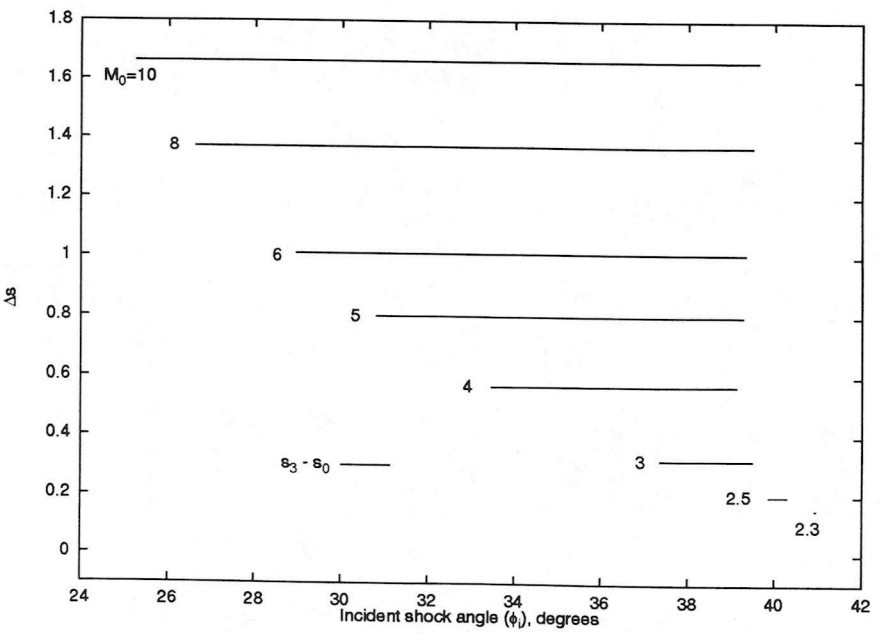

Figure 2.11: *Entropy increase across Mach stem part of MR in dual solution domain*

of Mach numbers M_0. Each curve extends from the von Neumann ($\phi_i = \phi_i^N$) to the detachment ($\phi_i = \phi_i^D$) condition. Note that for each M_0, $(s_3 - s_0)$ is greater than both $(s_{2,RR} - s_0)$ and $(s_{2,MR} - s_0)$. Note also that at the von Neumann condition $(s_{2,RR} - s_0)$ and $(s_{2,MR} - s_0)$ are identical (because the Mach stem has vanished) and that $(s_{2,RR} - s_0)$ increases more sharply with incident shock angle i.e.

$$\frac{d\,(s_{2,RR} - s_0)}{d\phi_i} \;>\; \frac{d\,(s_{2,MR} - s_0)}{d\phi_i}$$

For $\phi_i < \phi_i^N$ (i.e. where an IMR is theoretically possible) this trend continues since $\phi_{r,MR}$ must be greater than the corresponding $\phi_{r,RR}$ in order to achieve the negative flow deflection. As a consequence for $\phi_i < \phi_i^N$ the entropy increase across both parts of the MR is greater than that across the corresponding RR. This can be written as

$$\begin{aligned} (s_3 - s_0)^{\phi_i < \phi_i^N} &> (s_{2,RR} - s_0)^{\phi_i < \phi_i^N} \\ (s_{2,MR} - s_0)^{\phi_i < \phi_i^N} &> (s_{2,RR} - s_0)^{\phi_i < \phi_i^N} \end{aligned} \tag{2.14}$$

The expression (2.12) for the rate of entropy production for an oblique shock is adapted here for the entropy production rates for regular and Mach reflection

$$\dot{S}_{RR} = \int_{J_{r,RR}} \rho_{2,RR} u_{2,RR} \sin\left(\phi_{r,RR} - \theta_{r,RR}\right) (s_{2,RR} - s_0) dw_{r,RR} \tag{2.15}$$

$$\begin{aligned} \dot{S}_{MR} = &\int_{J_{r,MR}} \rho_{2,MR} u_{2,MR} \sin\left(\phi_{r,MR} - \theta_{r,MR}\right) (s_{2,MR} - s_0) dw_{r,MR} \\ &+ \int_{J_m} \rho_0 u_0 (s_3 - s_0) dw_m \end{aligned} \tag{2.16}$$

where $J_{r,RR}$, $J_{r,MR}$, J_m are the shapes of $\mathbf{r}$ (in RR and MR) and $\mathbf{m}$ respectively; $dw_{r,RR}$, $dw_{r,MR}$ and dw_m are their respective differential line elements. Note that in these expressions all sources of entropy production other than the incident shock, reflected shock and Mach stem are neglected. The total mass flow rate for a given M_0 and ϕ_i must be equal for RR and MR. However, not all of the flow is processed by

the shock system (see Figure 2.6). We make the assumption that the same amount of flow is processed by our simplified models of the RR and MR systems. This is exactly true at the von Neumann condition and appears to be a good approximation in the vicinity of this condition from flow visualisations [16],[17],[23]. This assumption provides a continuity equation

$$\int_{J_{r,RR}} \rho_{2,RR} u_{2,RR} \sin\left(\phi_{r,RR} - \theta_{r,RR}\right) dw_{r,RR} \;=$$

$$\int_{J_{r,MR}} \rho_{2,MR} u_{2,MR} \sin\left(\phi_{r,MR} - \theta_{r,MR}\right) dw_{r,MR} + \int_{J_m} \rho_0 u_0 dw_m \qquad (2.17)$$

From equations (2.15) and (2.16) the entropy production rate is the product of mass flow rate and entropy increase integrated across the shock system. Since the entropy increase across both parts of the IMR is greater than across the RR (see the inequalities (2.14)) and the total mass flow rate is the same in each case (see equation (2.17)), then we can conclude that the IMR entropy production rate is greater than the RR, regardless of the proportions of the total mass flow being processed by by the MR components. This is stated as

$$\left(\dot{S}_{MR}\right)^{\phi_i < \phi_i^N} \;>\; \left(\dot{S}_{RR}\right)^{\phi_i < \phi_i^N}$$

Hence by the principle of minimum entropy production RR is the observed solution.

The possibility of suppressing the RR to obtain the IMR does not violate this result for the same reasons as discussed in Section 2.6.1. In the present case for a fixed M_0 and ϕ_i both IMR and RR could occur from oblique shock theory but the principle selects RR. However if the downstream pressure is given as a boundary condition then the set of boundary conditions has changed and the principle does not apply. According to Hornung[23], if RR is impeded by setting the downstream pressure to a high value then IMR may occur, explaining the results of Henderson[25] where IMR was observed.

2.6.4 Shock Reflection Hysteresis

As discussed in Section 2.5, the persistence of MR in the dual solution domain i.e. for one half of the hysteresis loop has yet to be fully explained. In this section it will be argued that the MR may have a lower entropy production rate than the RR, and hence by the principle of minimum entropy production MR is the observed solution.

Figures 2.10 and 2.11 show the calculated entropy increases across a regular reflection ($s_{2,RR} - s_0$) and the oblique ($s_{2,MR} - s_0$) and Mach stem ($s_3 - s_0$) parts of a Mach reflection within the dual solution domain. From these figures it is evident that within the dual solution domain the entropy increase across the oblique part of the MR is less than that across the RR, but the entropy increase across the Mach stem is greater. This can be written as

$$\begin{aligned} (s_3 - s_0)^{\phi_i^N < \phi_i < \phi_i^D} &> (s_{2,RR} - s_0)^{\phi_i^N < \phi_i < \phi_i^D} \\ (s_{2,MR} - s_0)^{\phi_i^N < \phi_i < \phi_i^D} &< (s_{2,RR} - s_0)^{\phi_i^N < \phi_i < \phi_i^D} \end{aligned} \tag{2.18}$$

We would like to compare RR and MR entropy production rates. In this case to do this we must also examine the relative proportions of mass flow processed by each MR component. Expressions for $\dot{S}_{RR}$ and $\dot{S}_{MR}$, the rates of entropy production for RR and MR respectively, are given by equations 2.15 and 2.16. If we make the further assumption that these shocks are straight then the expressions simplify to

$$\dot{S}_{RR} = \rho_{2,RR} u_{2,RR} \sin(\phi_{r,RR} - \theta_{r,RR}) (s_{2,RR} - s_0) l_{r,RR} \tag{2.19}$$

$$\dot{S}_{MR} = \rho_{2,MR} u_{2,MR} \sin(\phi_{r,MR} - \theta_{r,MR}) (s_{2,MR} - s_0) l_{r,MR} + \rho_0 u_0 (s_3 - s_0) l_m \tag{2.20}$$

where $l_{r,RR}$, $l_{r,MR}$, and l_m are the lengths of $\mathbf{r}$ (in RR and MR), and $\mathbf{m}$ respectively.

To help us examine this, we define **A**, **B** and **C** as follows

$$\begin{aligned} \mathbf{A} &= \rho_{2,RR} u_{2,RR} \sin\left(\phi_{r,RR} - \theta_{r,RR}\right)\left(s_{2,RR} - s_0\right) \\ \mathbf{B} &= \rho_0 u_0 \left(s_3 - s_0\right) \\ \mathbf{C} &= \rho_{2,MR} u_{2,MR} \sin\left(\phi_{r,MR} - \theta_{r,MR}\right)\left(s_{2,MR} - s_0\right) \end{aligned} \tag{2.21}$$

then equations (2.15) and (2.16) become respectively

$$\begin{aligned} \dot{S}_{RR} &= \mathbf{A} l_{r,RR} \\ \dot{S}_{MR} &= \mathbf{B} l_m + \mathbf{C} l_{r,MR} \end{aligned} \tag{2.22}$$

Figure 2.12 shows the variation of the parameters **A**, **B** and **C** with ϕ_i within the dual solution domain for a free-stream Mach number $M_0 = 4.96$ for which $\phi_i^N = 30.9^o$. The significance of this particular condition is explained later. As illustrated in Figure 2.7 a feature of the von Neumann condition is that the length of the Mach stem **m** has become vanishingly small; the RR and MR are effectively identical ($l_m = 0, \phi_{r,RR} = \phi_{r,MR}$). This can be seen in Figure 2.10 where $\mathbf{A}(\phi_i^N) = \mathbf{C}(\phi_i^N)$ as a consequence. On increasing ϕ_i, **A** increases more quickly than **C**. Within the dual solution domain the principle of minimum entropy production has the potential for allowing selection of the prevailing reflection type. However, as is clear from equations (2.19) and (2.20), knowledge of the shock wave lengths as well as the quantities **A**,**B**,**C** is required in order to make a direct comparison between $\dot{S}_{RR}$ and $\dot{S}_{MR}$. Introducing a relationship between the total mass flow rates through the RR and MR aids clarification. Assuming that the mass flow through the RR is the same as that through the MR and that the shocks are straight, equations (2.19) and (2.20) become

$$\rho_{2,RR} u_{2,RR} \sin\left(\phi_{r,RR} - \theta_{r,RR}\right) l_{r,RR} = \rho_0 u_0 l_m + \rho_{2,MR} u_{2,MR} \sin\left(\phi_{r,MR} - \theta_{r,MR}\right) l_{r,MR} \tag{2.23}$$

We want to show that MR is the observed solution by the principle of minimum entropy production i.e.

$$\dot{S}_{RR} > \dot{S}_{MR} \tag{2.24}$$

Combining this condition with equations (2.21),(2.22) and (2.23) gives a geometric condition for the prevalence of MR in the dual solution domain in terms of the gasdynamic conditions

$$\frac{l_m}{l_{r,RR}} < \frac{\rho_{2,RR} u_{2,RR} \sin\left(\phi_{r,RR} - \theta_{r,RR}\right)\left(s_{2,RR} - s_{2,MR}\right)}{\rho_0 u_0 \left(s_3 - s_{2,MR}\right)} \tag{2.25}$$

It is not possible to evaluate the LHS of this expression using the present analysis. Experimental results for shock reflection hysteresis at $M_0 = 4.96$ have been presented in [17]. The same problem has also been studied numerically [18],[19],[29]. From these results it is possible to extract a value for $l_m/l_{r,RR}$ within the dual solution domain and test the condition (2.25). However, it is useful to recap on how this expression was obtained. In particular, two important simplifying assumptions have been made:

The total mass flow rate through the RR and MR are equivalent. As shown in Figure 2.6 the expansion around the trailing edge of the wedge interacts with the reflected shock wave. Some of the flow which is processed by the incident shock is not processed by the reflected shock. As the Mach stem grows the inclination and length of the reflected oblique shock changes. As a result, the proportion of the flow processed by the reflected oblique shock is different for RR and MR.

Sources of entropy production other than shock waves are neglected. The entropy production due to the interacton of the reflected shock with the expansion is assumed to be equivalent for RR and MR i.e. does not influence comparisons of

entropy production rates.

The errors associated with these assumptions increase on departing from the von Neumann condition. They are difficult to quantify; from flow visualisations [16], [17],[23] the lengths of the reflected shocks in the dual solution domain do not appear to differ greatly for RR and MR but this does not provide sufficient justification for identifying some range of ϕ_i in the vicinity of ϕ_i^N for which condition (2.25) is valid, even before taking into account errors associated with measuring l_m and $l_{r,RR}$. It is therefore difficult to investigate whether the condition (2.24) is true for even one particular set of conditions.

Directly comparing $\dot{S}_{RR}$ and $\dot{S}_{MR}$ on a reliable basis using the present approach is therefore not possible. However, it is still possible to make use of the fact that our assumptions are exact at the von Neumann condition. If condition (2.24) is true for the dual solution domain then the condition

$$\left(\frac{d\dot{S}_{RR}}{d\phi_i}\right)^{\phi_i=\phi_i^N} > \left(\frac{d\dot{S}_{MR}}{d\phi_i}\right)^{\phi_i=\phi_i^N} \tag{2.26}$$

must also hold since

$$\left(\dot{S}_{RR}\right)^{\phi_i=\phi_i^N} = \left(\dot{S}_{MR}\right)^{\phi_i=\phi_i^N} \tag{2.27}$$

Noting that for MR any increase in the mass flow through the Mach stem due to its growth entails a corresponding reduction in the mass flow through the reflected shock i.e.

$$\frac{d}{d\phi_i}(\rho_{2,MR}u_{2,MR}\sin(\phi_{r,MR}-\theta_{r,MR})\,l_{r,MR}) + \frac{d}{d\phi_i}(\rho_0 u_0 l_m) = 0 \tag{2.28}$$

then after some manipulation equations (2.19),(2.20) and (2.26) yield

$$\frac{d}{d\phi_i}(s_{2,RR}-s_0) > \frac{d}{d\phi_i}(s_{2,MR}-s_0) + \frac{\rho_0 u_0(s_3-s_{2,MR})}{\rho_{2,RR}u_{2,RR}\sin(\phi_{r,MR}-\theta_{r,MR})l_{r,RR}}\frac{dl_m}{d\phi_i} \tag{2.29}$$

which is valid only at the von Neumann condition. If h_{in} is the distance between the leading edges of the two symmetric wedges ($h_{in}/2$ is then the distance from the wedge leading edge to the symmetric line/reflecting surface in Figure 2.6) then we have simply

$$\frac{dl_m}{d\phi_i} = \frac{h_{in}}{2}\frac{d(\frac{l_m}{h_{in}/2})}{d\phi_i}$$

Equation (2.29) then becomes

$$\frac{d}{d\phi_i}(s_{2,RR} - s_0) > \frac{d}{d\phi_i}(s_{2,MR} - s_0) + \frac{\rho_0 u_0 (s_3 - s_{2,MR})(h_{in}/2)}{\rho_{2,RR} u_{2,RR} \sin(\phi_{r,MR} - \theta_{r,MR}) l_{r,RR}} \frac{d(\frac{l_m}{h_{in}/2})}{d\phi_i} \tag{2.30}$$

The quantity $\rho_0 u_0 (h_{in}/2)$ is the total mass flow rate between the wedge and the symmetric line. The quantity $\rho_{2,RR} u_{2,RR} \sin(\phi_{r,MR} - \theta_{r,MR}) l_{r,RR}$ is the total mass flow rate across the reflected oblique shock. Their ratio, which we denote $ratio_{flow}$, can be estimated from experiment along with the quantity $d(\frac{l_m}{h_{in}/2})/d\phi_i$. All other quantities in this expression can be obtained from our simplified analysis. The quantities pertaining to condition (2.30) for the von Neumann condition $M_0 = 4.96$, $\phi_i^N = 30.9^o$ are summarised in Table 2.1. Note that the necessary geometric values extracted from experimental data are deliberately estimated on the side of a high RHS to this condition in order to avoid uncertainty in this conclusion[1,2]. From this analysis the condition (2.30) is demonstrated to be true, and therefore condition (2.24) is true in the vicinity of the von Neumann condition for $M_0 = 4.96$.

Note that for the experiment referred to here the dual solution domain was found to terminate a few degrees before the detachment condition. It is possible that at this point the condition (2.24) is no longer true. An observation from [17] which supports this is that $d(\frac{l_m}{h_{in}/2})/d\phi_i$ increases on departing from the von Neumann condition. The present simplified approach is not adequate to conclusively demonstrate whether

the principle of minimum entropy production can explain the persistence of MR as part of the hysteresis loop. However, the above result can at least be regarded as evidence which supports this idea. A conclusive analysis would require at least accurate experimental measurement of shock wave lengths. An alternative approach could be to directly measure the entropy production from numerical results.

$\frac{d}{d\phi_i}(s_{2,RR} - s_0)$	1.2478
$\frac{d}{d\phi_i}(s_{2,MR} - s_0)$	0.6675
$(s_3 - s_{2,MR})$	0.5116
$ratio_{flow}$	3.3333[1]
$\frac{d}{d\phi_i}(\frac{l_m}{h_{in}/2})$	0.2843[2]
LHS of (2.30)	1.248
RHS of (2.30)	1.152

Table 2.1: *Values for condition (2.30) at* $M_0 = 4.96$, $\phi_i^N = 30.9^o$

2.7 Discussion

In this section the principle of minimum entropy production has been applied to some shock wave and shock reflection phenomena in an attempt to explain experimental observations. First, the conclusions of other authors who examined supersonic flow deflection and regular shock reflection were restated to establish that a precedent for this type of approach exists. It was then demonstrated how the principle can be used to explain why the well known von Neumann criterion marks one limit of the shock reflection dual solution domain and Inverted Mach Reflection is not normally observed. It is then suggested that the phenomenon of shock reflection hysteresis

[1]This estimate is taken from the flow visualisations in [17]. From these images between 40% and 50% of the total mass flow is processed by the reflected oblique shock. Here a value of 30% is assumed to ensure a valid conclusion.

[2]Estimated from the straight line part of Figure 10(a) in [17]. Using the least-squares fit would yield a smaller value.

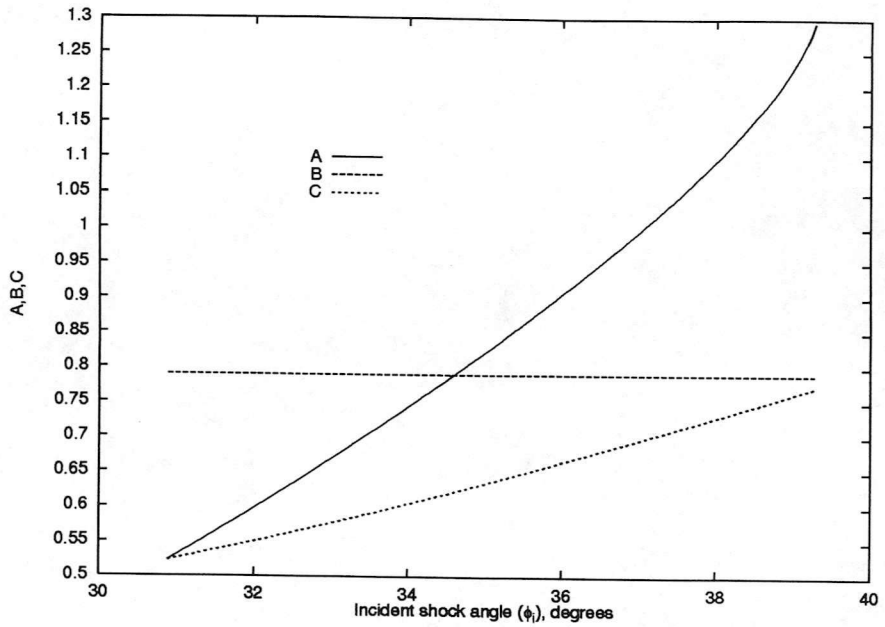

Figure 2.12: *Variation of parameters* **A**,**B**,**C** *in dual solution domain for* $M_0 = 4.96$

has yet to be full explained; that the principle of minimum entropy production may provide an explanation for the persistence of Mach reflection when the dual solution domain is approached from a Mach reflection condition is proposed. The difficulties associated with applying the principle to this problem are discussed. Some evidence supporting this theory is presented for one particular hysteresis case for which experimental data is available. Some recommendations are made for continued study of this problem.

Chapter 3

Numerical Method

3.1 Flow Solver

In this chapter, it is described how an axisymmetric (laminar) Navier-Stokes flow solver has been used to study the phenomenon of shock reflection hysteresis in an underexpanded jet. The results of this study will be examined in the light of the understanding of the two-dimensional hysteresis phenomenon established in Chapter 2. The main features of the flow solver are outlined here. For full details see [34],[35],[36].

A cell-centred finite volume method is employed. Osher's scheme and MUSCL variable interpolation are used to discretise the convective terms and central differencing for the diffusive terms. The linear system arising at each implicit time step is solved using a Generalised Conjugate Gradient method. A Block Incomplete Lower-Upper (BILU) factorisation is used as a preconditioner. A structured multi-block grid system is employed. The BILU factorisation is decoupled between blocks to reduce communication. This results in efficient implementation on distributed memory parallel computers. An important feature of the flow solver is the use of approximate Jacobian matrices for the left hand side of the linear system. This has led to substantial reductions in memory and CPU-time requirements compared to the use

of exact Jacobians.

For this study it is assumed throughout that the working gas is in the continuum regime with no condensation and has constant specific heats. These assumptions are verified in a straightforward manner. The extremities of pressure, temperature etc. experienced in the experiments can be obtained from [2]. The Knusden number based on the shock cell length was calculated [37] [38] as being less than 0.15 at all times. The continuum Navier-Stokes equations hold up to Knusden numbers of 0.2 [39] so we are just within the continuum regime. Based on the experiments reported in [40] the present cases are also condensation free. Despite the high Mach numbers and strong shock waves encountered in the experiments the gas temperature remained relatively low at all times, well below the levels where molecular dissociation or vibrational excitation become important [39]. These assumptions are confirmed by the Hypersonic Aerodynamics Group at DERA Farnborough where the experiments were carried out.

3.2 Boundary Conditions

Figure 3.1 shows a diagram of the computational domain with labelled boundary condition types (the size of the nozzle is exaggerated for clarity). The boundaries labelled A denote adiabatic wall boundaries with no slip and zero normal pressure gradient. At B a symmetry condition was applied. To decide which boundary conditions to apply at C we have the advantage that across all of this boundary we know that we should have outflow. In keeping with an inviscid characteristic analysis, the flow variables are extrapolated from the interior of the domain except for the case of locally subsonic outflow where the pressure was imposed at the background level. Two alternative treatments were tested and rejected. First, all of the flow variables were extrapolated across all of the boundary. This significantly

impaired convergence in regions of subsonic outflow. Secondly, the background pressure was imposed across all of the boundary. This did not impair convergence but did result in significant spurious oscillations in regions of supersonic outflow. The boundary condition treatment at the nozzle inlet D requires a somewhat more involved treatment. We know the reservoir stagnation conditions (denoted here by r) but require boundary conditions for the nozzle inlet i. This is achieved by assuming that the total enthalpy and entropy are the same for the reservoir and nozzle inlet, thus obtaining expressions for p_i and ρ_i which are imposed. The velocity components are extrapolated from the interior of the domain. Note that assuming constant entropy s implies a constant entropy measure S defined by

$$S = \frac{p}{\rho^\gamma}$$

For convenience the non-dimensionalisation is constructed such that

$$\rho_r = 1, \qquad p_r = \frac{1}{\gamma} \tag{3.1}$$

are the values of density and pressure respectively in the reservoir. The reservoir sound speed, total enthalpy and the entropy measure are then

$$a_r = 1, \qquad H_r = \frac{1}{(\gamma - 1)}, \qquad S_r = \frac{1}{\gamma}$$

We now have two conditions to impose at the inlet i :

$$H_r = \frac{\gamma p_i}{(\gamma - 1)\,\rho_i} + \frac{u_i^2 + v_i^2}{2}, \qquad S_r = \frac{p_i}{\rho_i^\gamma}$$

The velocity components u_i and v_i are extrapolated from the interior of the domain. The inlet density and pressure are then

$$\rho_i = \left[1 - \frac{u_i^2 + v_i^2}{2}(\gamma - 1))\right], \qquad p_i = \frac{1}{\gamma}\rho_i^\gamma$$

For the boundary condition treatment at E the background stagnation conditions are known but the flow direction is not known *a priori*. This being similar to the

nozzle inlet boundary treament, the boundary conditions here are treated in the same manner except that background conditions are used instead of reservoir conditions in equation 3.1.

It is possible to construct a Riemann invariant based boundary condition treatment for the boundaries at C and E analogous to that commonly used as a "far-field" condition for aerofoil flow studies. However the present approach was found to be adequate and its implementation straightforward in the framework of the existing flow solver. One more boundary condition was used; as described below, calculations were also carried out concerning only the nozzle flow. At the nozzle outlet, where the flow is supersonic except in the boundary layer, all flow variables were extrapolated from the interior of the domain.

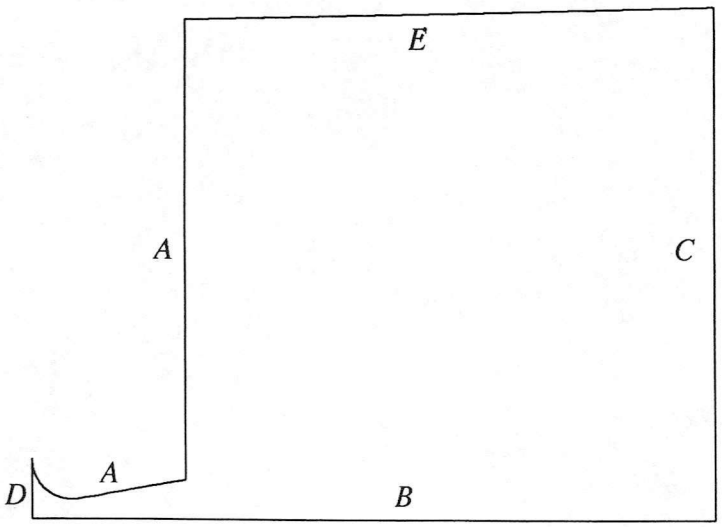

Figure 3.1: *Boundary conditions*

3.3 Initial Conditions and Pseudo-Steady Approach

As a first step to studying the full problem a preliminary calculation for the nozzle only was carried out. Using a linear variation from reservoir to Mach 3 conditions along the axis from the inlet to the outlet as initial conditions was found to considerably reduce the calculation time compared with using uniform reservoir or sonic conditions. The solution from this calculation was used as the initial solution in the nozzle for the main calculation, and the calculated nozzle exit conditions were used as the initial conditions for the domain directly downstream of the nozzle exit. For the remainder of the domain the background conditions were applied as initial conditions. Calculations were performed over a range of pressure ratios from well inside the regular reflection range to well inside the Mach reflection range including the hysteresis loop. A quasi-steady approach was employed in order to account for time history effects. First, converged solutions were obtained for the conditions at the extremities of the range of interest. These were used as initial solutions for a calculation with a small change in pressure ratio, thus beginning to traverse the range, this solution being used subsequently as the next initial solution etc. By using a small step change in pressure ratio between calculations this approach is very robust and converges quickly at each condition, as shown in Figure 3.2. Here it should be noted that the scaling residual used in the figure, the residual after the first step, is already small. A reduction of just over two orders of magnitude in the residual was found to be sufficient for the step size used. Further convergence did not alter the solution. This usually required around 100 steps to achieve[1] but may require up to 500 steps when a switch in shock reflection type occurs. By contrast, obtaining a converged solution (without the aid of a close initial solution) for the end points of the pressure ratio range is far more demanding, requiring approxim-

[1] corresponding to a CPU time of 950 seconds on a 200MHz Intel Pentium Pro processor

ately 30 times the computational effort. The step change in pressure ratio used is 2.857, corresponding to a step change in reservoir stagnation pressure of 0.1 *torr* for a background pressure of 35 *mtorr* in terms of the original experiments.

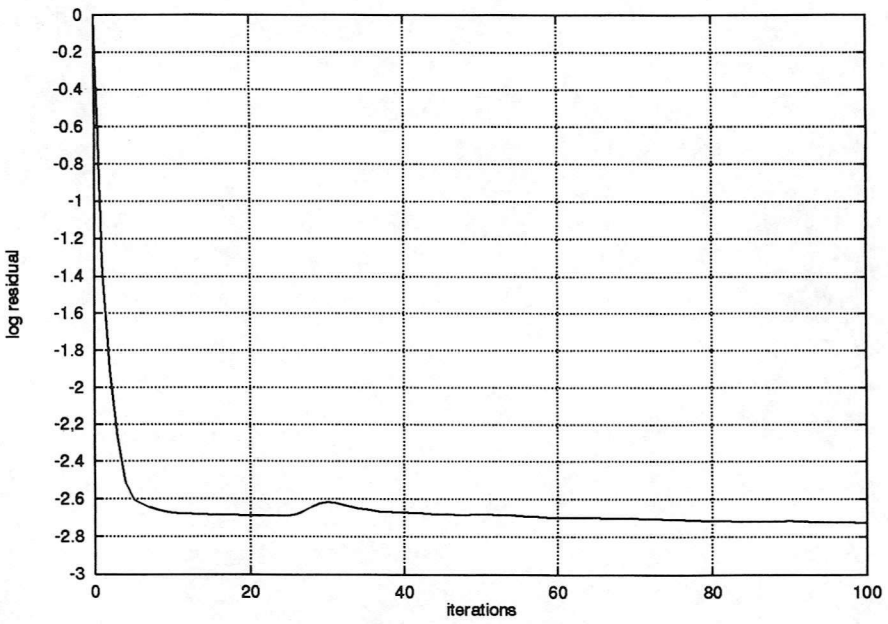

Figure 3.2: *Convergence behaviour at each step*

3.4 Grid

The grid generation for this case is straightforward due to the simple geometry. The computational domain extends 70 nozzle throat diameters downstream in order to capture at least two shock cells and 20 diameters radially from the symmetric line. The grid within the nozzle consists of 58 and 21 points in the axial and radial directions respectively, this number having been determined from a grid convergence study carried out independently of the plume calculations. The plume calculations were also performed using a number of grids. The effect of the radial extent of the computational domain was examined by comparing results for calculations with grids extending 20 and 40 nozzle throat diameters from the symmetric line. The results are identical, see for example Figure 3.3. It was also found that the grid

density in the radial direction can be surprisingly coarse compared to the axial direction, 65 points being sufficient. In order to obtain a grid converged solution, the necessary axial grid density was much finer. Results were obtained for three different levels of axial grid fineness, see Table 3.1. Using the grid convergence measure of the calculated limits of the hysteresis loop, a grid converged solution was obtained using 937 points in the axial direction. Centre-line values were also checked for grid convergence, see Figure 3.4. For any given pressure ratio the grid is excessively fine in places, but since the location of the shock reflections vary widely with pressure ratio and the same grid was used in each case this was unavoidable.

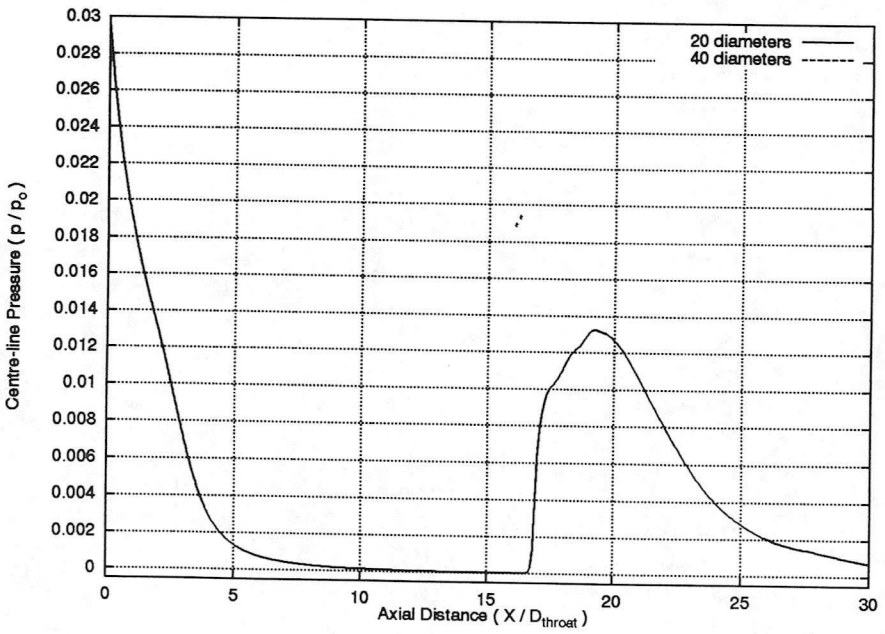

Figure 3.3: *Effect of radial extent of domain for* $p_o/p_b = 285.7$

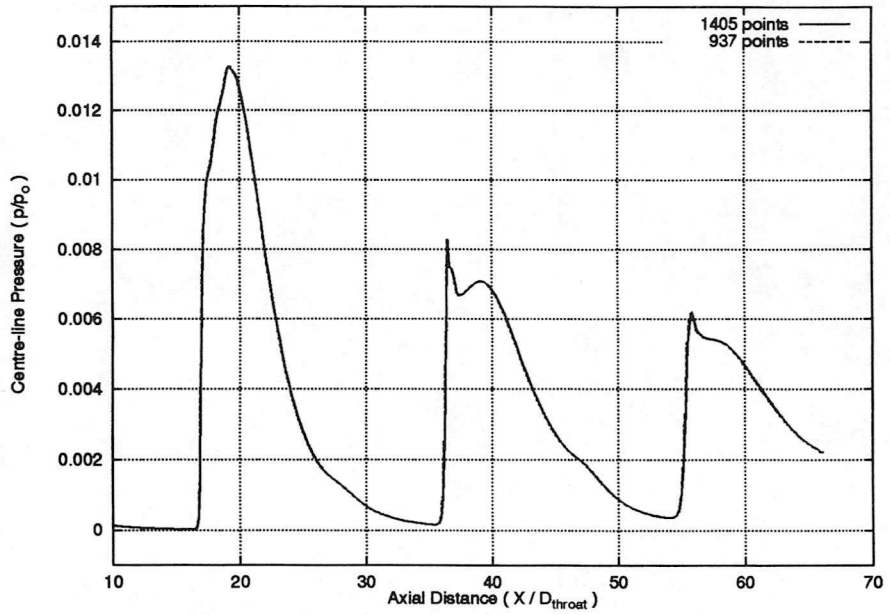

Figure 3.4: *Result of grid convergence study for* $p_o/p_b = 285.7$

No. points along axis	*Lower limit*[2]		*Upper limit*[3]	
	p_o/p_b	X/D_{throat}	p_o/p_b	X/D_{throat}
469	200.0 || 202.9	14.10 || 13.14	434.3 || 437.1	21.02 || 18.81
937	214.3 || 217.1	14.55 || 13.41	334.3 || 337.1	18.32 || 16.50
1405	214.3 || 217.1	14.55 || 13.41	334.3 || 337.1	18.32 || 16.50

Table 3.1: *Grid independence study for hysteresis loop*

[2]first value is highest pressure ratio not on MR curve, second is lowest ratio in loop
[3]first value is highest pressure ratio in loop, second is lowest ratio not on RR curve

Chapter 4

Results

4.1 Nozzle Calculations

Welsh[2] describes a series of experiments where the effect of varying the ratio of reservoir stagnation pressure p_o to background pressure p_b on the plume of a highly underexpanded nitrogen jet is examined. The reported shock reflection hysteresis phenomenon provided the motivation for this CFD study. In the experiments p_o was varied and p_b was kept constant. In this way the nozzle exit conditions as well as the pressure ratio were varied. In addition, experiments were carried out for a number of values of p_b and for two different nozzle sizes. It is difficult then to isolate the effect of the varying pressure ratio. For these reasons, as a preliminary to the nozzle-plume study, it is useful to perform calculations for the nozzle alone in order to examine the effect of the nozzle Reynolds number on the nozzle exit conditions. This will help to put subsequent nozzle-plume calculations and comparison with experiment in their proper context.

Calculations were performed for a range of reservoir stagnation pressures, from 2 *torr* to 70 *torr*, covering the range used in the experiments. The reservoir stagnation temperature T_o is constant at 288.0K and the two throat diameters used are 5.19 *mm* and 15.3 *mm*. The Reynolds number based on throat conditions Re_t can

then be calculated for each p_o, assuming sonic conditions at the throat, using the isentropic relations and Sutherland's law for viscosity. The variation of Re_t with pressure ratio for each nozzle is shown in Figure 4.1. The present CFD method was then used to obtain results for the nozzle flow for a range of Re_t.

The calculated variation of the maximum nozzle exit Mach no. M_{exit} with throat Reynolds number Re_t is shown in Figure 4.2. Calculated pressure contours for Re_t= 800 are shown in Figure 4.3. As expected, as Re_t decreases so does M_{exit}, caused by the displacement effect of the boundary layer decreasing the effective area of the divergent section of the nozzle. The thickness of the boundary layer can be visualised from the Mach number plot Figure 4.4. The magnitude of the trend confirms that for each of the experiments the nozzle exit conditions vary significantly.

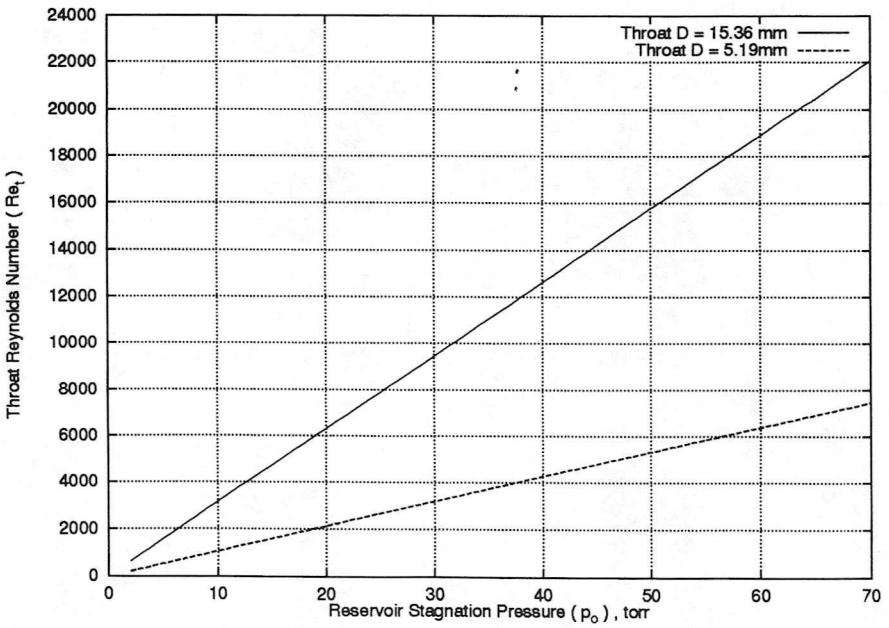

Figure 4.1: *Reynolds number variation with stagnation pressure*

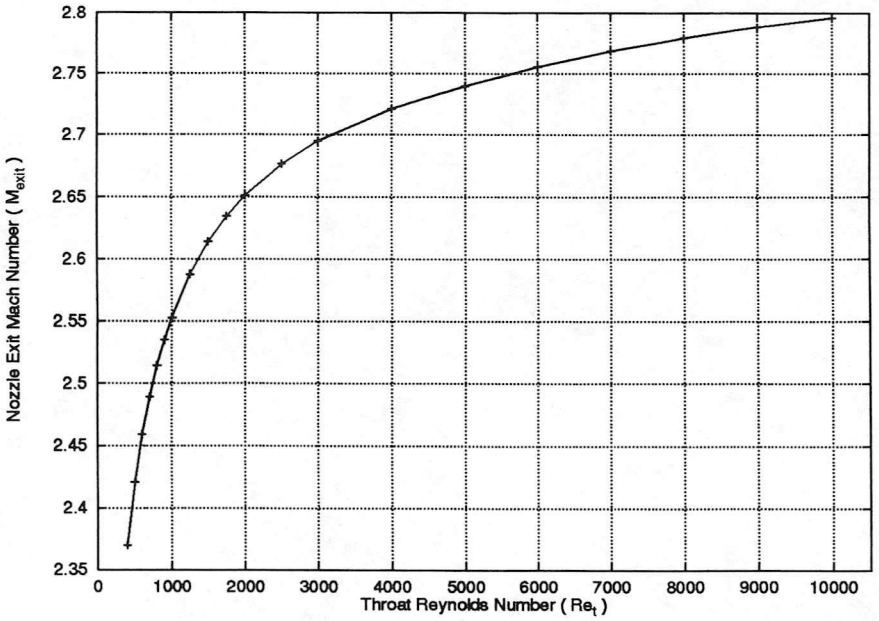

Figure 4.2: *Effect of throat Reynolds number on maximum nozzle exit Mach number*

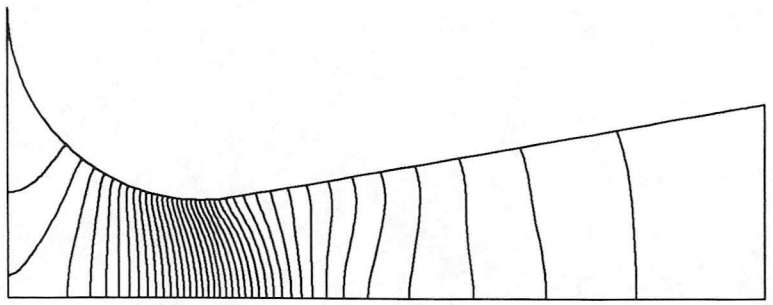

Figure 4.3: *Pressure contours, nozzle calculation,* $Re_t = 800.0$

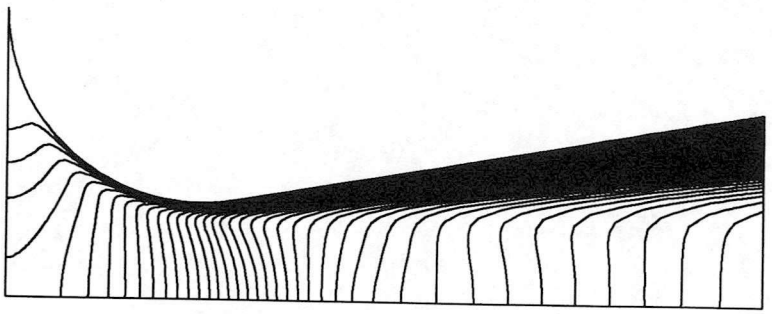

Figure 4.4: *Mach number contours, nozzle calculation, $Re_t = 800.0$*

4.2 Hysteresis Loop

The calculated shock reflection type and distance variation with pressure ratio is shown in Figure 4.5. The Reynolds number was kept constant, as discussed below. The shock reflection distance is the axial distance (X_r) from the nozzle exit to the centre of the first centre-line regular reflection or Mach disc, non-dimensionalised with respect to the nozzle throat diameter (D_{throat}). The figure shows how for a small range of pressure ratios either regular reflection (RR) or Mach reflection (MR) may occur. Which condition prevails depends on the time history of the plume development, in accordance with experimental observation. Selecting, for example, the pressure ratio value of 300 in Figure 4.5, the corresponding point on the RR(MR) curve will be reached if the condition immediately prior was also on the RR(MR) curve. The arrows on the figure indicate the "flip" in reflection type which occurs at the limits of the hysteresis loop. From this figure it can be concluded that the

quasi-steady approach (Section 3.3) has been successful, at least qualitatively, in modelling the shock reflection hysteresis phenomenon. A description of the plume structures associated with RR and MR is included in Section 4.3.

Figure 4.6 shows the extent of the calculated hysteresis loops compared with the data from experiments [2]. The scatter in the experimental results should be explained. Each experiment was carried out with a constant background pressure and varying reservoir stagnation pressure, with the result that the nozzle Reynolds number is not constant. This is illustrated in Figure 4.1 which shows the effect of the varying stagnation pressure on the throat Reynolds number for the nozzles used in the experiment. The effect of a varying nozzle Reynolds number on the maximum exit Mach number for these nozzles is shown in Figure 4.2. Thus for each of the experiments it is difficult to examine the effect of a varying pressure ratio when the Reynolds number and nozzle exit conditions are not constant.

With this is mind, the present calculations were performed with a constant throat Reynolds number of 4000 and a varying pressure ratio, which in effect models varying background pressure and constant nozzle conditions, thus enabling examination of the pressure ratio influence independently. Although we cannot expect close agreement with the experiments for this reason, we can at least conclude from Figure 4.6 that our present calculation of the location of the hysteresis loop is reasonable in terms of both pressure ratio and reflection distance. The calculated Mach number on the axis immediately upstream of the first shock reflection is plotted in Figure 4.7 for a number of representative points in the pressure ratio range. Within the dual solution domain, a higher Mach number is reached before the shock reflection in the regular reflection cases. This trend is discussed in Section 4.3.4.

In Section 2.4 it is described how in the case of two dimensional shock reflection hysteresis the limits of the dual solution domain can be calculated from knowledge of the Mach number upstream of the reflection and the incident shock angle. In principle a similar analysis is possible here; the Mach number and local shock angle can be obtained from the CFD results, and the theoretical limits to the dual solution domain calculated and compared with the numerical results. However, this approach was not successful since the shock angles are difficult to measure accurately from field plots due to curvature of the shock and shock smearing. Other aspects of the analysis of the computational results are also hampered by this problem, as discussed in Section 4.3.3.

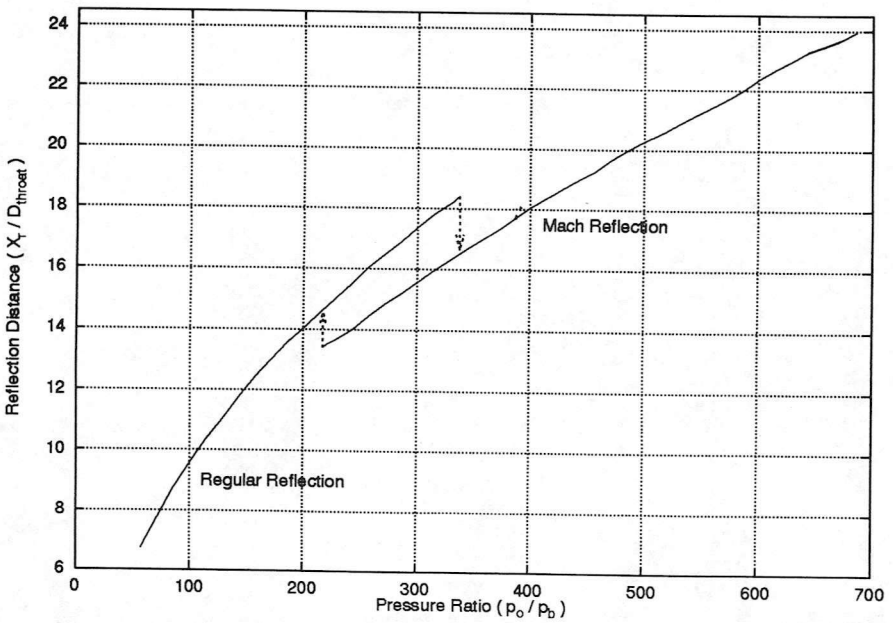

Figure 4.5: *Distance to reflection for range of pressure ratios,* $Re_t = 4000$

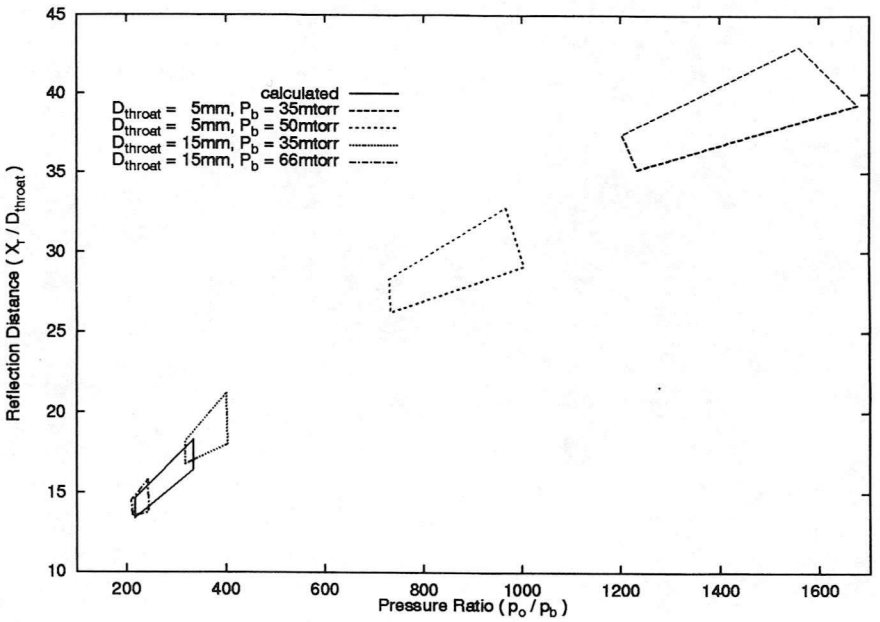

Figure 4.6: *Location of hysteresis loops, experiments and computation*

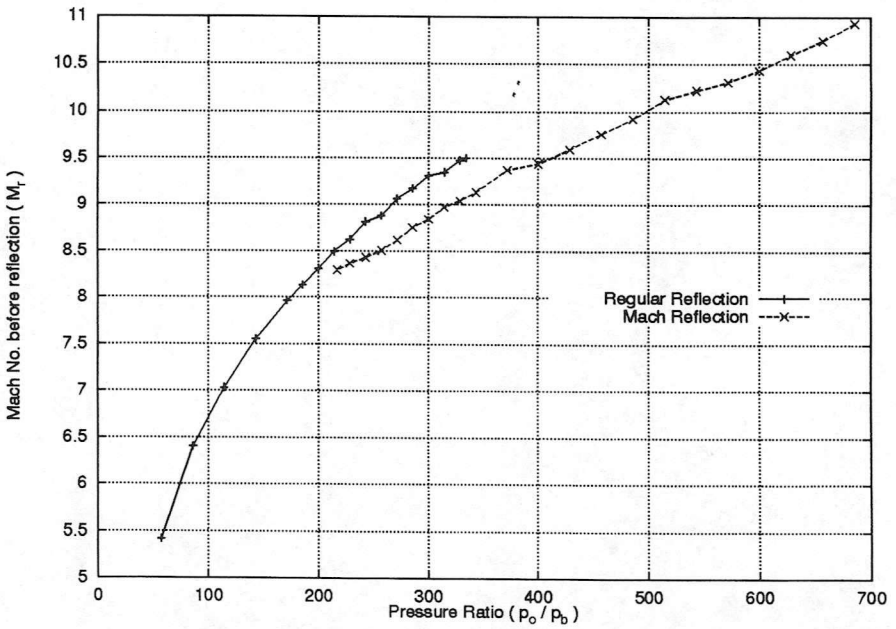

Figure 4.7: *Mach no. before reflection for range of pressure ratios,* $Re_t = 4000$

4.3 Plume Structure

4.3.1 Presentation of Results

It is useful here to include a note on the sequence in which the results are presented. The figures appear out of sequence when referenced from the text; this is because all of the field plots (whether for RR or MR) are grouped together, followed by the centre-line plots, in this way aiding comparison of figures.

4.3.2 Regular Reflection

Figure 4.8 shows calculated density contours for a pressure ratio $P_o/P_b = 185.7$ which lies in the regular reflection range. The figure clearly shows the repeated shock cell pattern typical of this regime. Figures 4.9 to 4.11 show a detail of the second shock cell including the incident shock from the first cell and reflected shock at the beginning of the third. Pressure contours, Mach contours, velocity vectors and streamlines are shown. For clarity velocity vectors are shown for only every fifth grid cell in the axial direction and every fourth in the radial direction. From these field plots the important elements of the plume structure can be visualised. On exiting from the nozzle (on the left hand side of Figure 4.8) the air is at a higher pressure than the ambient air and expands sharply, increasing the cross-sectional area of the plume. Expansion waves reflect from the free jet boundary as compression waves, and in so doing turn the jet boundary towards the axis. The curved nature of the jet boundary causes the compression waves to coalesce and form an oblique shock wave, the incident shock labelled. Air passing through this shock is turned back towards the axis and collects in a shock layer of increasing density, causing the shock itself to turn further towards the axis. This is also encouraged by the increasing Mach number of the air before the shock in the still expanding core flow, whose pressure now lies below the background pressure. The axisymmetric shock intersects the axis and is reflected as another oblique shock. This Regular

Reflection is analogous to the Regular Reflection in two dimensional uniform flow discussed in Chapter 2. The shock reflection is the mechanism through which the condition of axial flow on the centre-line is achieved; after the incident shock the flow is converging on the axis and is then turned away by the reflected shock. The flow direction can be clearly seen from the streamlines in Figure 4.11. Immediately downstream of the reflection point the air being processed by the reflected shock is of increasing density due to the accumulated shock layer, turning the shock towards the axis. This tendency is quickly overtaken by the rapidly re-expanding core flow which causes the shock to turn outwards again towards the jet boundary. The change in curvature of the reflected shock is best seen in Figure 4.9. The shock is reflected as expansion waves by the free jet boundary which is turned back away from the axis. This expansion reinforces the expansion of the under-expanded core flow, and initiates another shock cell when the expansion waves again reflect from the jet boundary. The pattern is repeated, its strength gradually lessening, until the structure is destroyed by diminishing pressure ratio and mixing.

Figures 4.20 to 4.24 show calculated centre-line distributions of pressure, density, Mach number, axial velocity and temperature. Regular reflections arising for three pressure ratios are shown; $p_o/p_b = 334.3$ is the highest pressure ratio for which regular reflection occurs (a limit of the hysteresis loop), $p_o/p_b = 57.1$ was the lowest pressure ratio considered and $p_o/p_b = 185.7$ was selected as an intermediate point. The ragged peaks to the pressure and density curves for the lower pressure ratio cases are possibly explained by the interaction of the shock layer behind the incident shock with the reflected shock. It is interesting to note that upstream of the interactions all of the curves are coincident. Despite the fact that the cross-sectional area of the plume increases with pressure ratio, the core expansion along the axis appears to be independent of pressure ratio until the reflection occurs. From Figure 4.22

it can be seen that the flow behind the first regular shock reflection may become subsonic. From the present calculations, the lowest pressure ratio at which this occurs is $p_o/p_b = 171.4$ and as the pressure ratio increases in the regular reflection range the subsonic region becomes larger and the minimum Mach number smaller. At the upper limit of the RR range ($p_o/p_b = 334.3$) the subsonic region is 2.65 throat diameters in length with a minimum Mach number of 0.26 . More will be said about the region of subsonic flow in Section 4.3.5.

4.3.3 Mach Reflection

As the ratio of nozzle exit to background pressure increases, the amount of expansion at the nozzle exit increases and the shock cell grows in size. As the pressure ratio increases, the angle at which the incident shock intersects the axis increases. This is a trend which is evident from comparison of contour plots for various pressure ratios, but the actual angle is difficult to measure precisely due to the curvature of the shock and its apparent thickness in the CFD results due to shock smearing. The increasing angle has the result that the flow behind the incident shock is deflected more towards the centre-line. The stronger incident shock also results in a greater decrease in Mach number across the shock, an effect which is countered by a greater Mach number in the core flow upstream of the incident shock, as shown in Figure 4.7. The shock deflection angle necessary for a reflected shock to re-align the flow is thus increasing, and at the same time the Mach number between shocks may be decreasing. A point is reached where an oblique shock solution for the required θ given M_1 is not possible. The re-alignment is in this case achieved via a Mach reflection, which consists of a normal shock called a Mach disc and a curved oblique shock, see Figures 4.12 to 4.15. The flow is subsonic behind the Mach disc, but is supersonic behind the oblique shock. These areas are separated by a slip line which emanates from the triple point where all three shocks meet. Downstream of the

Mach disc, the flow re-expands to become supersonic and initiates a second shock cell in a similar fashion to the case of regular reflection. As the pressure ratio is increased further, the shock cell grows in size, and the incident shock angle upstream of the triple point continues to steepen. This Mach Reflection is analogous to the Mach Reflection in two dimensional uniform flow discussed in Chapter 2.

A recirculation zone was predicted behind the Mach disc, see for example Figures 4.15 and 4.16. This surprising result was first reported by Martin Gilmore at DERA Farnborough for an as yet unpublished single calculation in the MR region. This feature is predicted in the present results for all the pressure ratios examined in the MR range. As can be seen from Figures 4.13 and 4.25, immediately downstream of the Mach disc the pressure is still increasing; this pressure gradient appears to be driving the recirculation. An explanation for the continuing increase in pressure is that immediately downstream of the Mach disc the gas being processed by the reflected oblique shock is of relatively high density due to the accumulation in the incident shock layer.

The calculated Mach disc is curved, convex if viewed from upstream, for each of the pressure ratio values examined. The amount of curvature increases slowly with pressure ratio. The curvature is apparent in Figures 4.13 and 4.14. This curvature implies that the flow is being turned away from the axis at the triple point. This corresponds to an Inverted Mach Reflection following Hornung's classification [21]. However, due to the curvature of all three shocks and their apparent thickness in the present results it is difficult to precisely identify the location of the triple point and verify the Mach Reflection type. The flow direction changes significantly in the locality of the triple point, see Figure 4.16.

Figures 4.25 to 4.29 show calculated centre-line distributions of pressure, density, Mach number, axial velocity and temperature. Mach reflection results for three pressure ratios are shown; $p_o/p_b = 217.1$ is the lowest pressure ratio for which Mach reflection occurs (the lower limit of the hysteresis loop), $p_o/p_b = 685.7$ was the highest pressure ratio considered and $p_o/p_b = 342.9$ was selected as an intermediate point. As also shown in the regular reflection results, upstream of the interactions all of the curves are coincident. From Figure 4.28 it can be seen that the flow behind the Mach disc reverses. At the lower limit of the hysteresis loop ($p_o/p_b = 217.1$) the subsonic region is 5.58 throat diameters in length. At the highest pressure ratio considered ($p_o/p_b = 685.7$) the subsonic region is 8.82 throat diameters in length.

The shock reflection type in the subsequent shock cells downstream of the first was calculated to be regular in all cases, as shown in Figure 4.27 where the flow is supersonic following the second (and third) sudden compressions. However, this study has concentrated on the first shock cell and no grid independence study was carried out for the other cells.

4.3.4 Dual Solution Domain

Figures 4.17 and 4.18 show calculated density contours for both MR and RR for the same pressure ratio ($p_o/p_b = 285.7$), a condition which lies in the dual solution domain. Note that upstream of the first shock reflection no difference in the flow behaviour can be detected. This point is supported by Figures 4.30 to 4.34 where centre-line distributions of pressure, density, Mach number, axial velocity and temperature are compared for the same calculations. Upstream of the first shock reflection the curves are coincident. It is also clearly shown in these figures that the MR occurs slightly upstream of the corresponding RR, allowing a greater initial expansion in the RR case.

4.3.5 Pseudo-Mach Reflection

There is some evidence to suggest that the regular reflections discussed in Section 4.3.2 are in fact Mach reflections with a Mach disc of small diameter. In Figure 4.10 there appears to be a slip line behind the 'regular' reflection; compare with the stream line behind the Mach reflection in Figure 4.14. As already noted in Section 4.3.2 there is a significant subsonic region behind the 'regular' reflections at the higher pressure ratios. However, it is unclear whether this apparent Mach reflection is physically correct or can be attributed to grid coarseness and/or an inappropriate spatial discretisation method. On close examination of the pressure contours in the region around the reflection (see Figure 4.9) there is an apparent Mach disc of approximately two grid cells in diameter. As discusssed in Section 3.4 the criterion used in the grid independence study is the calculated hysteresis loop limits and not the resolution of any particular flow feature. The ability of the spatial discretisation employed (Section 3.1) to resolve the reflection of oblique shocks is also unclear. As the pressure ratio is decreased, the flow behind the reflection becomes supersonic and the slip line indicated in the Mach number contour plots becomes less distinct. Figure 4.19 shows a Mach number contour plot similar to that in Figure 4.10 but for the lowest pressure ratio considered $p_o/p_b = 57.1$. The apparent slip line has faded entirely, the flow is supersonic behind the reflection, but it could still be argued that the reflected shock appears normal at the reflection. To ascertain whether the calculated pseudo-Mach reflections are in fact regular reflections or small diameter Mach reflections would require at the least a further grid refinement study.

Although there is doubt concerning the regular reflection resolutions at the reflection point, the possibility that two different levels of Mach reflection are occurring should not be discounted. Referring to the pressure-deflection diagrams introduced in Section 2.3 the situation is complicated because the incident shocks are in this

case curved. The condition (1) on the I polar could be in several different locations for the same incident shock because the deflection θ varies along the shock and conditions upstream of the shock are varying along its length. Consider an inverted Mach reflection, see Figure 2.2(f), in the underexpanded jet plume. As the pressure ratio is decreased from this condition the reflection type may suddenly change not to regular reflection but to an entirely different Mach reflection with a much smaller Mach disc. A possible location for the point (1) relative to its IMR location is at a greater θ value, corresponding to a longer incident shock which is steeper at the triple point and a smaller Mach disc. Such a reflection is represented in the (p, θ) plane by Figure 2.2(c). As discussed in Section 2.3, a dual solution domain can exist in the simpler case of the reflection of a straight, planar shock wave. Examination of the problem via (p, θ) diagrams does not provide information about the Mach stem length. Applied to the case of a curved incident shock this implies that multiple Mach reflection solutions are possible.

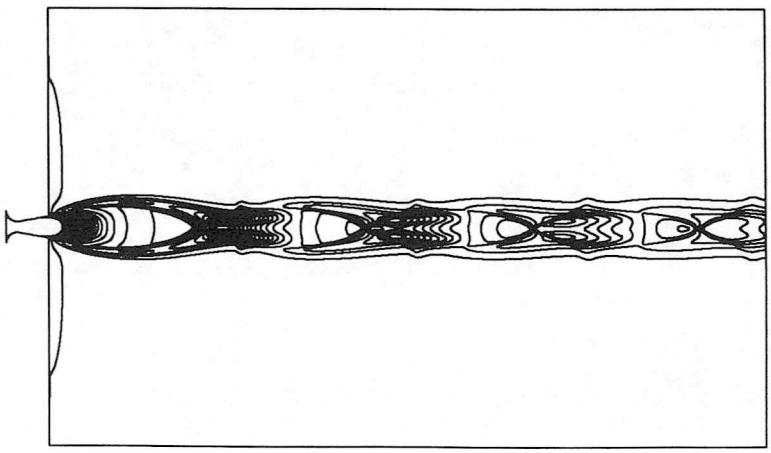

Figure 4.8: *Density contours showing regular reflection, $P_o/P_b = 185.7$*

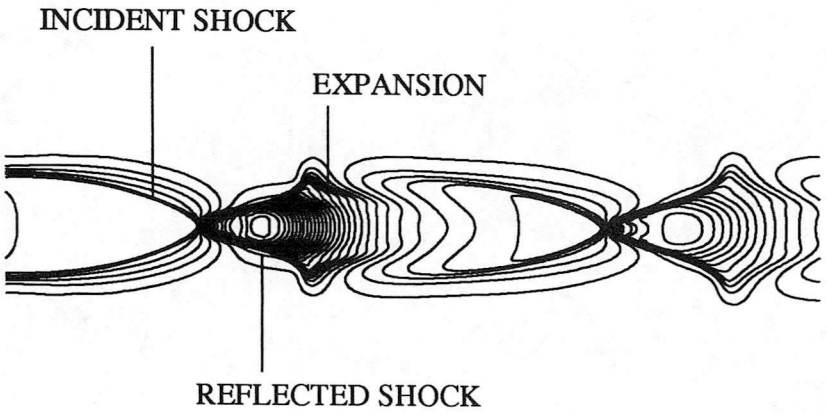

Figure 4.9: *Pressure contours showing regular reflection, $P_o/P_b = 185.7$*

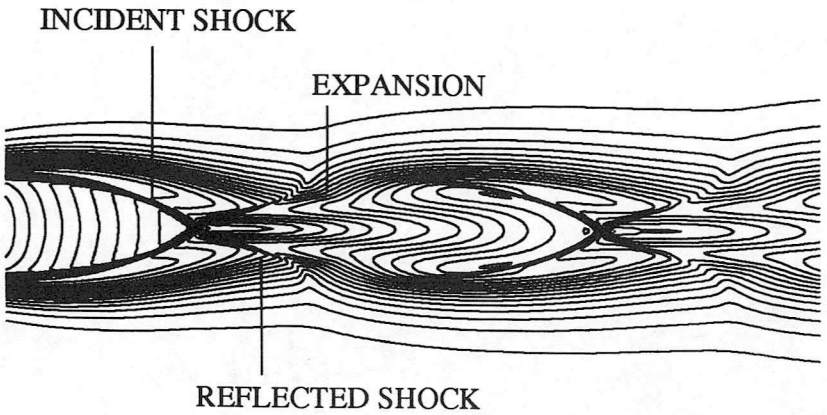

Figure 4.10: *Mach contours showing regular reflection, $P_o/P_b = 185.7$*

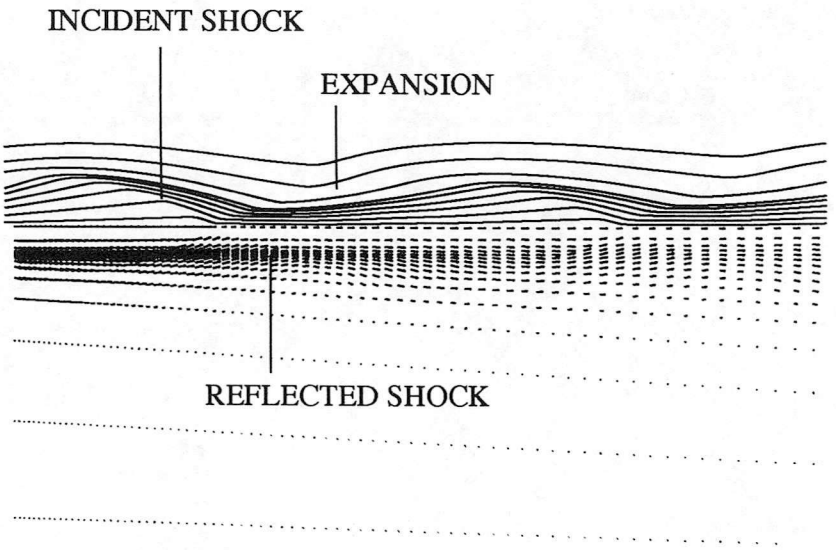

Figure 4.11: *Velocity vectors and streamlines showing regular reflection, $P_o/P_b = 185.7$*

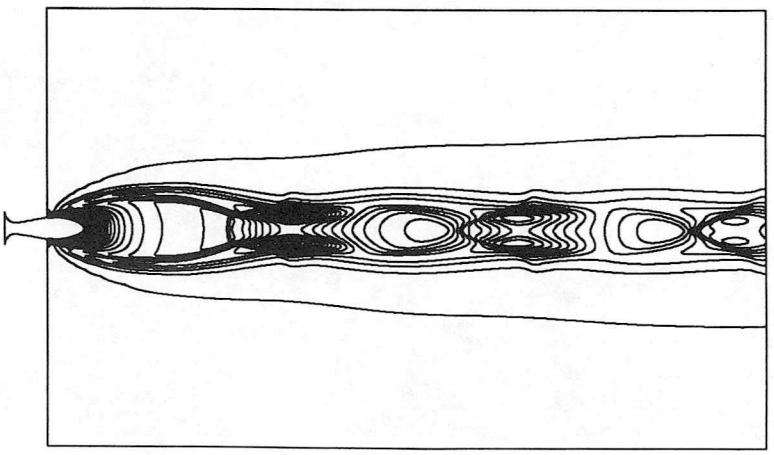

Figure 4.12: *Density contours showing Mach reflection, $P_o/P_b = 342.9$*

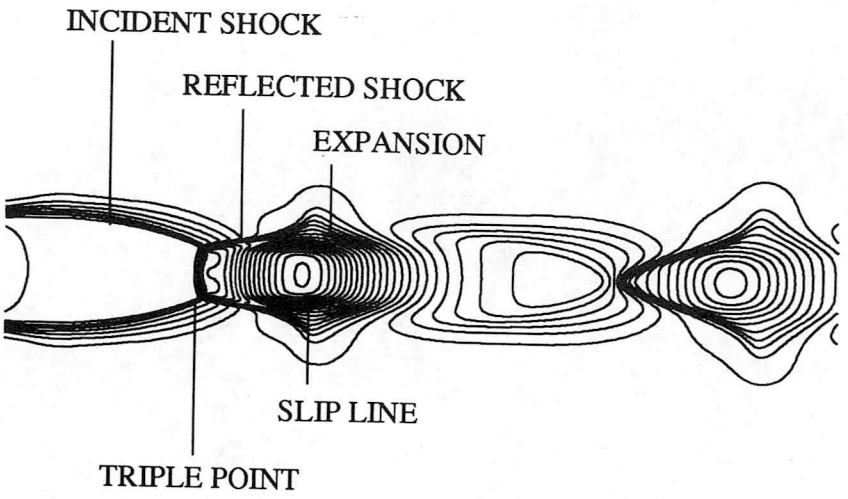

Figure 4.13: *Pressure contours showing Mach reflection, $P_o/P_b = 342.9$*

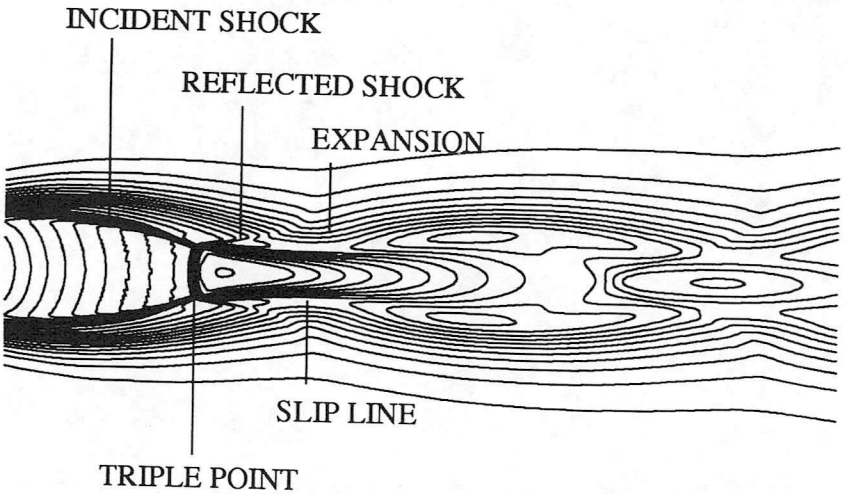

Figure 4.14: *Mach contours showing Mach reflection, $P_o/P_b = 342.9$*

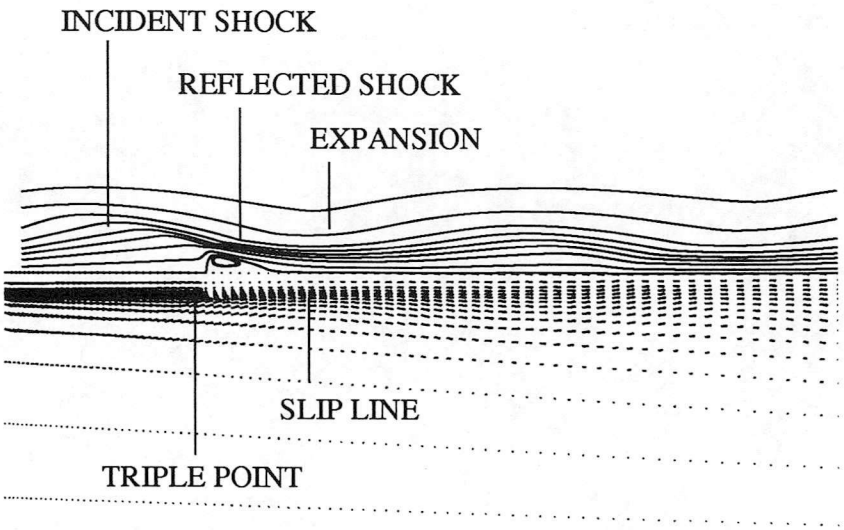

Figure 4.15: *Velocity vectors and streamlines showing Mach reflection,* $P_o/P_b = 342.9$

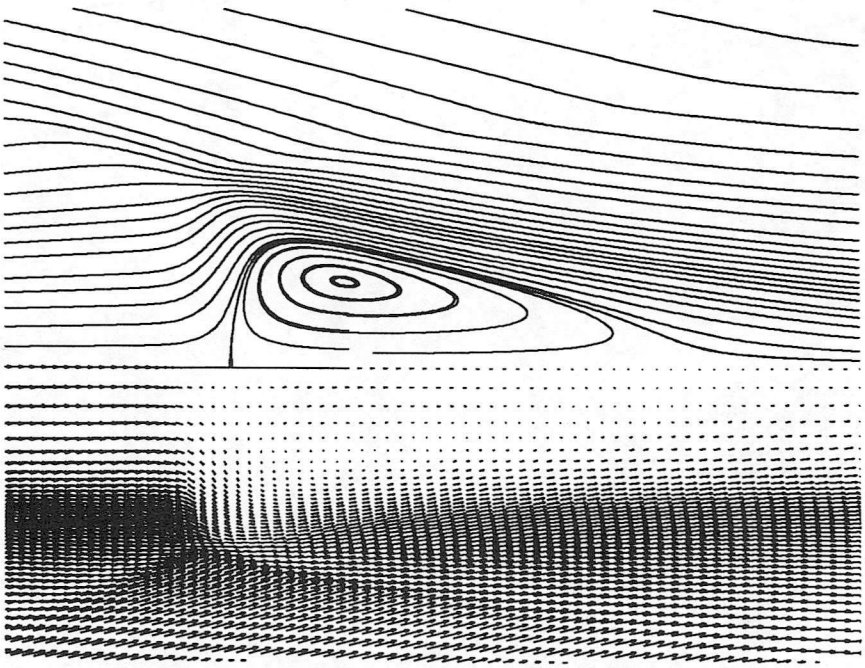

Figure 4.16: *Detail of velocity vectors and streamlines showing Mach reflection,* $P_o/P_b = 342.9$

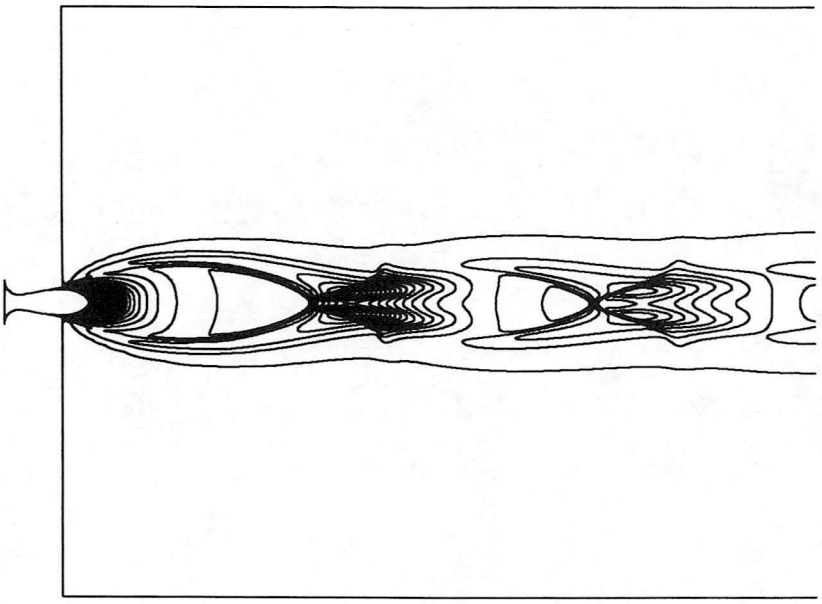

Figure 4.17: *Density contours showing regular reflection, $P_o/P_b = 285.7$*

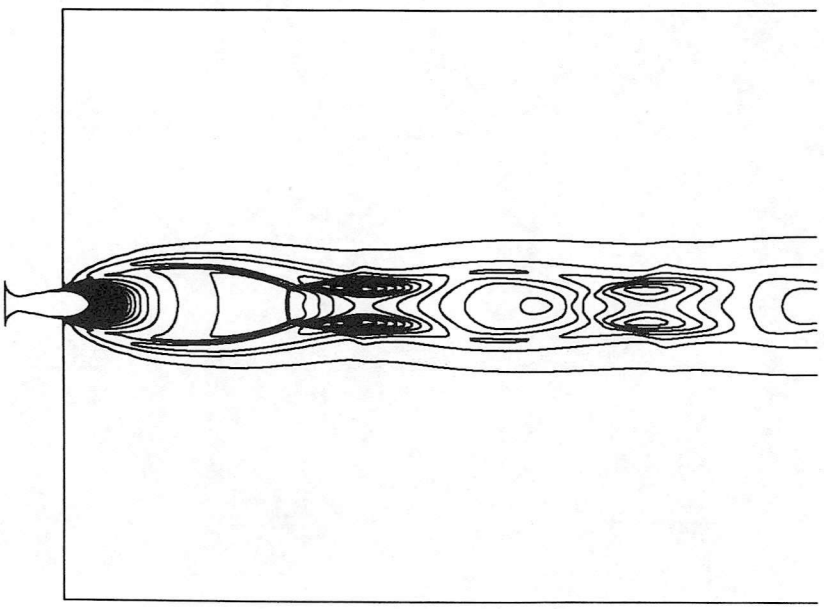

Figure 4.18: *Density contours showing Mach reflection, $P_o/P_b = 285.7$*

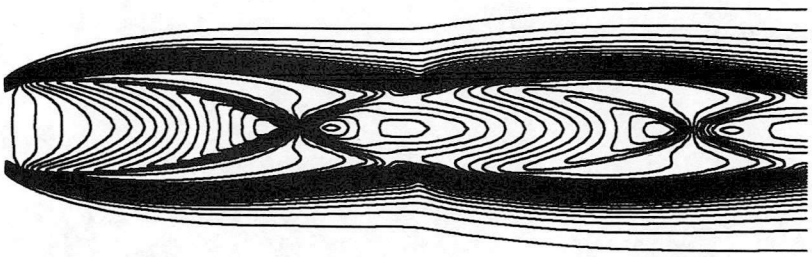

Figure 4.19: *Mach contours showing regular reflection, $P_o/P_b = 57.1$*

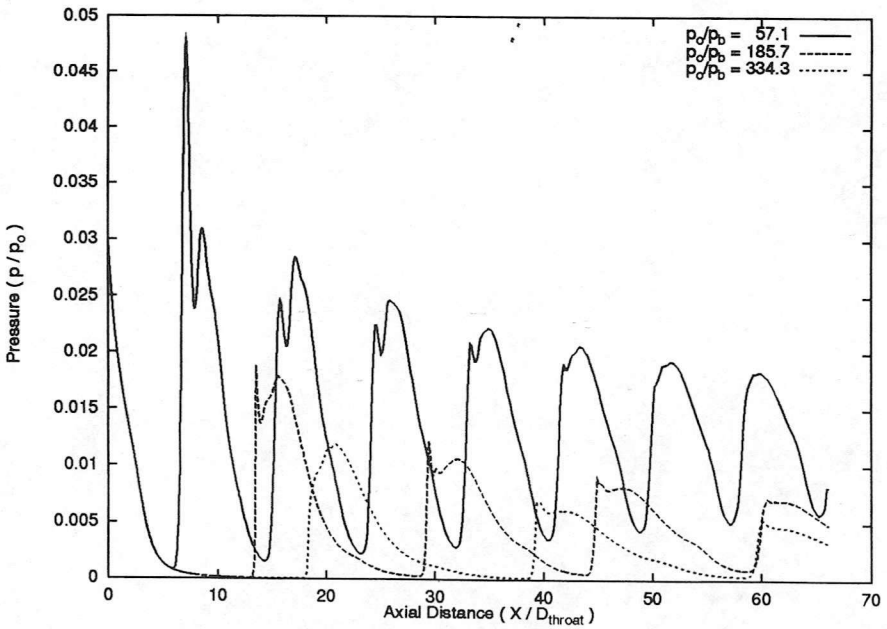

Figure 4.20: *Centre-line pressure distribution, regular reflection*

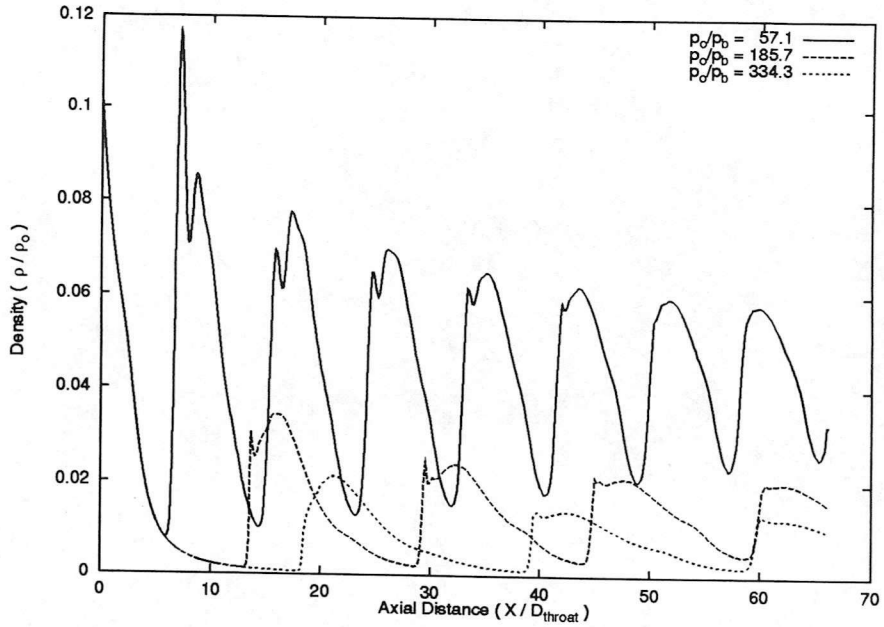

Figure 4.21: *Centre-line density distribution, regular reflection*

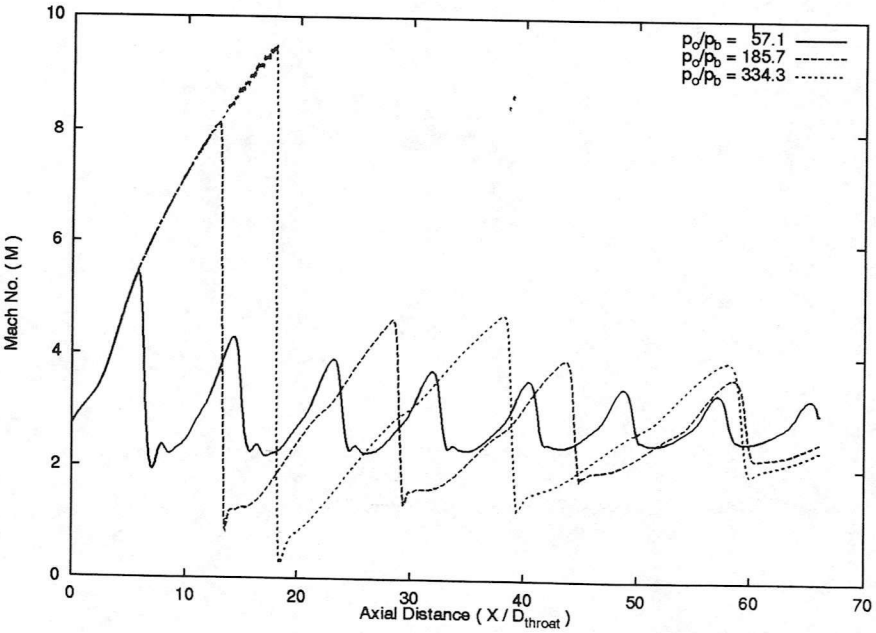

Figure 4.22: *Centre-line Mach no. distribution, regular reflection*

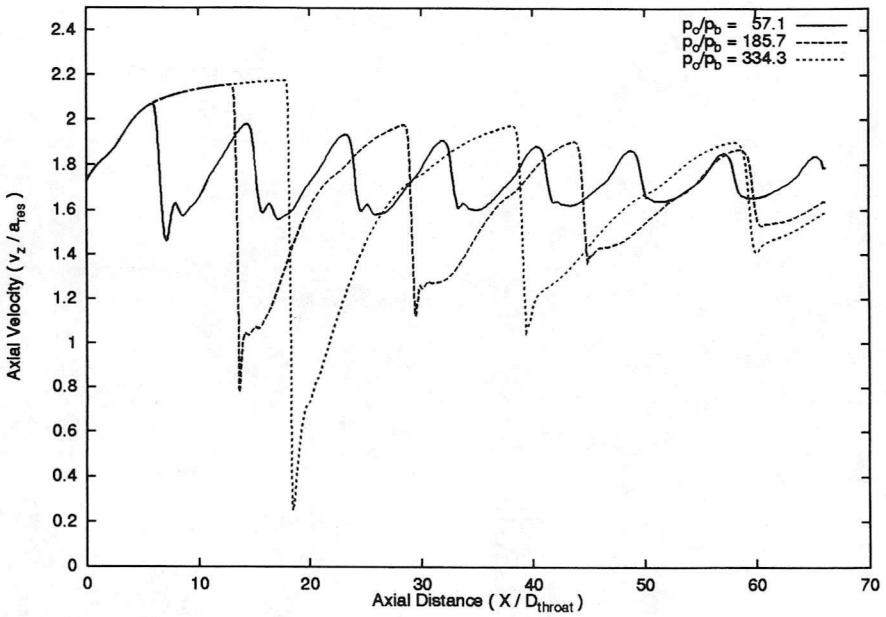

Figure 4.23: *Centre-line axial velocity distribution, regular reflection*

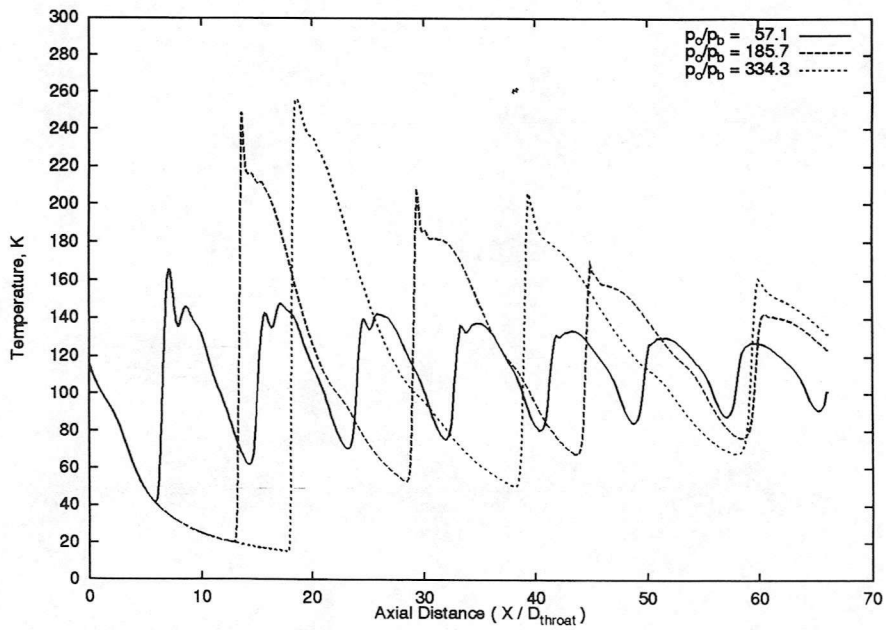

Figure 4.24: *Centre-line temperature distribution, regular reflection* $T_o = 288.0\ K$

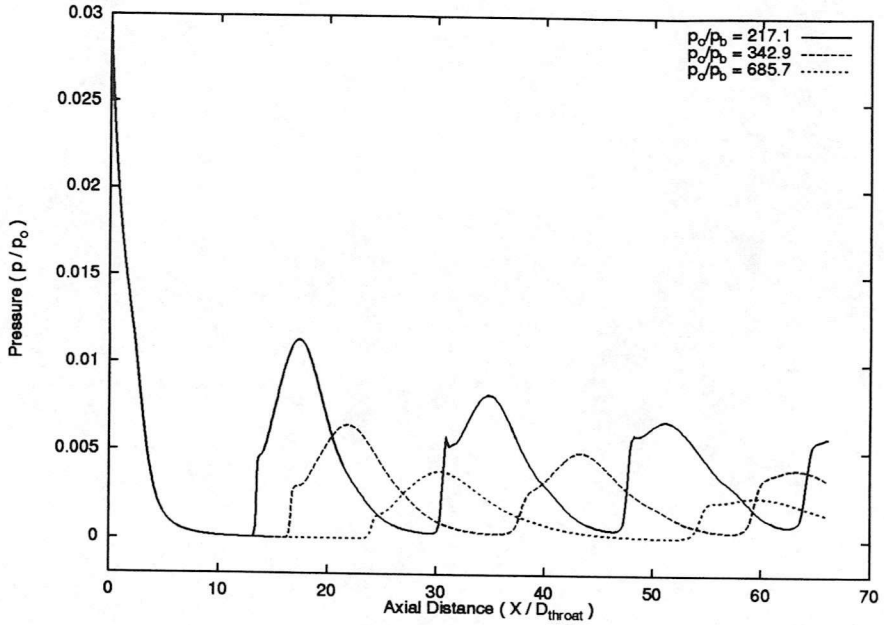

Figure 4.25: *Centre-line pressure distribution, Mach reflection*

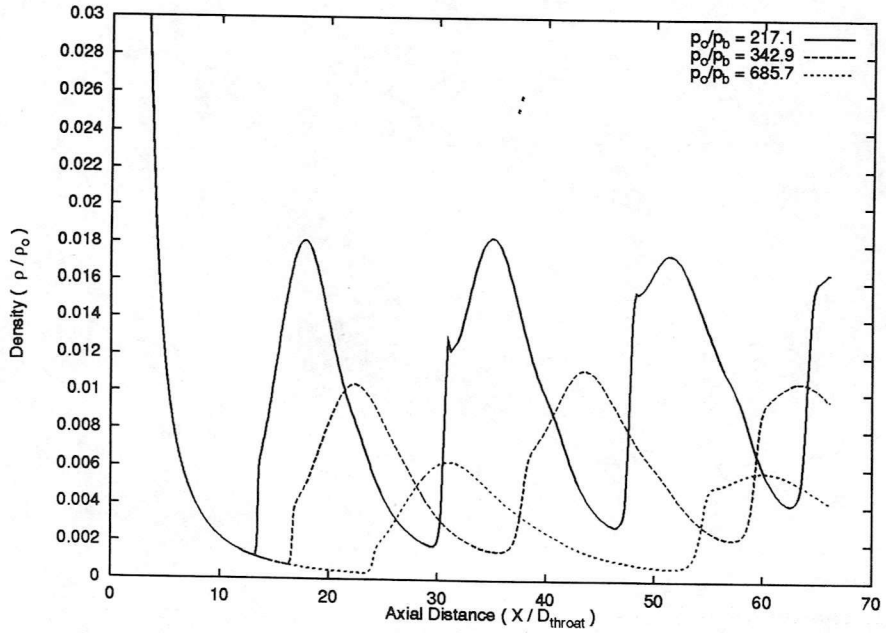

Figure 4.26: *Centre-line density distribution, Mach reflection*

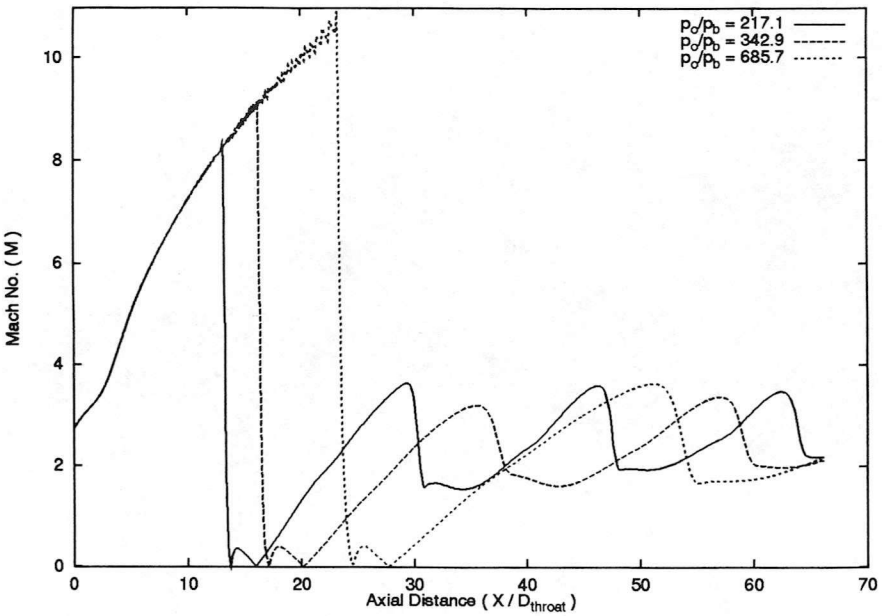

Figure 4.27: *Centre-line Mach no. distribution, Mach reflection*

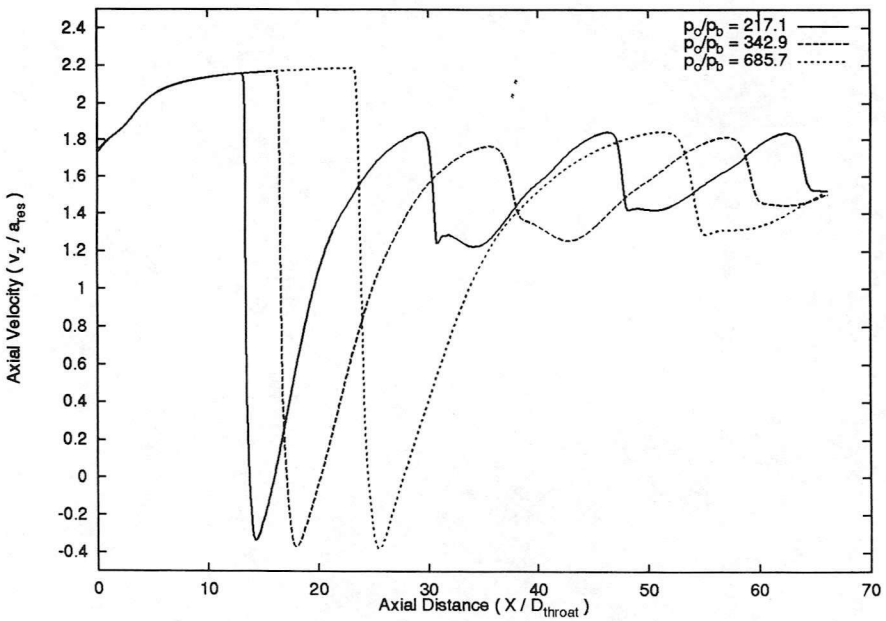

Figure 4.28: *Centre-line axial velocity distribution, Mach reflection*

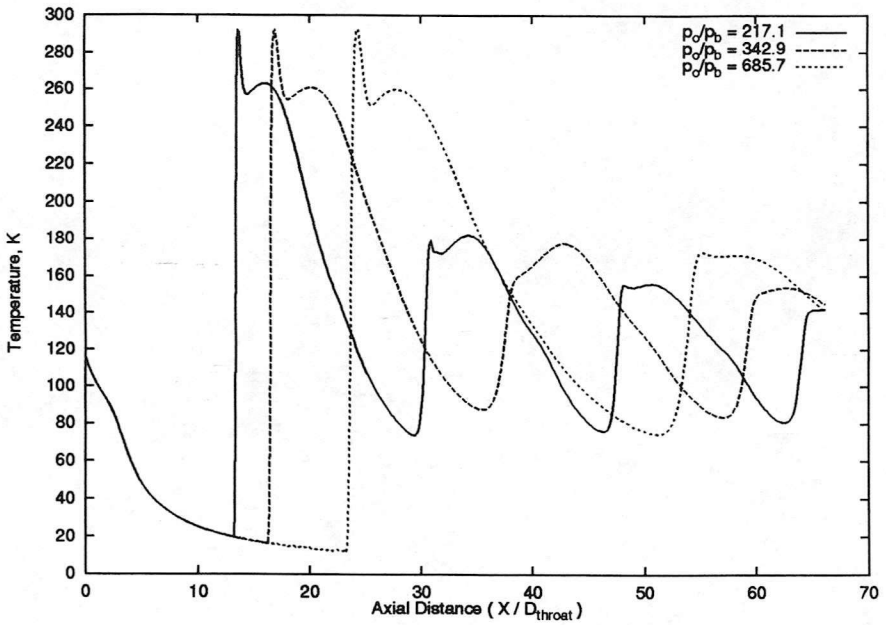

Figure 4.29: *Centre-line temperature distribution, Mach reflection* $T_o = 288.0\ K$

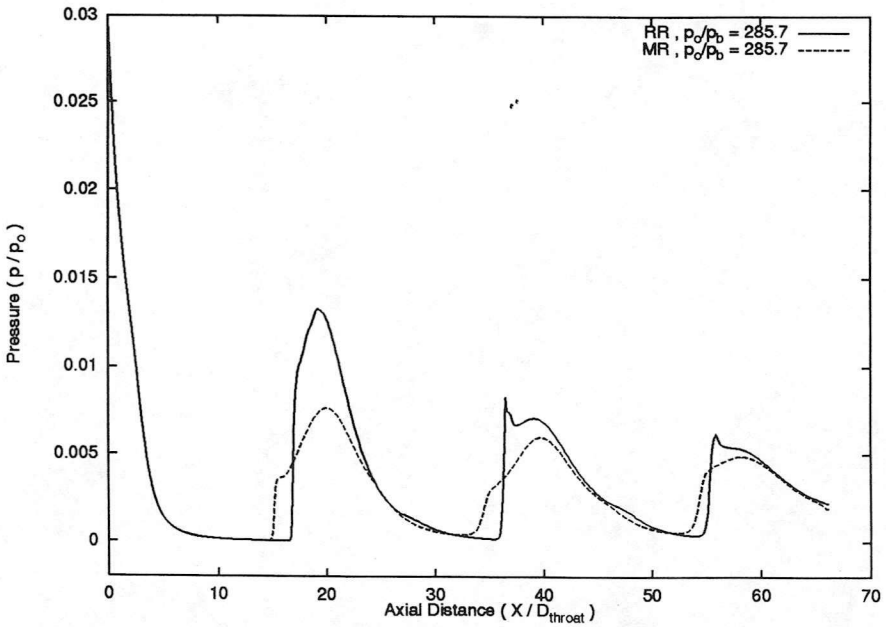

Figure 4.30: *Centre-line pressure comparison, regular and Mach reflection*

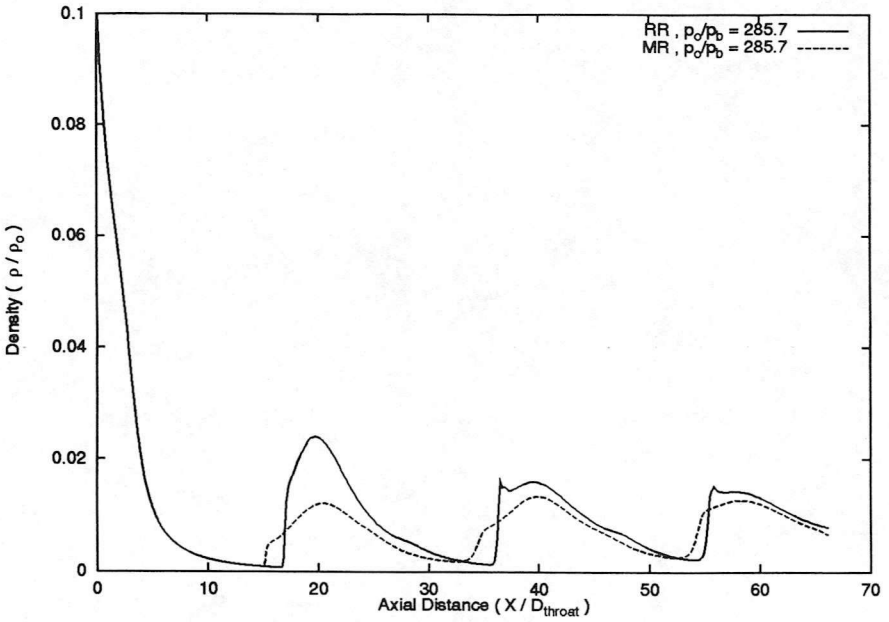

Figure 4.31: *Centre-line density comparison, regular and Mach reflection*

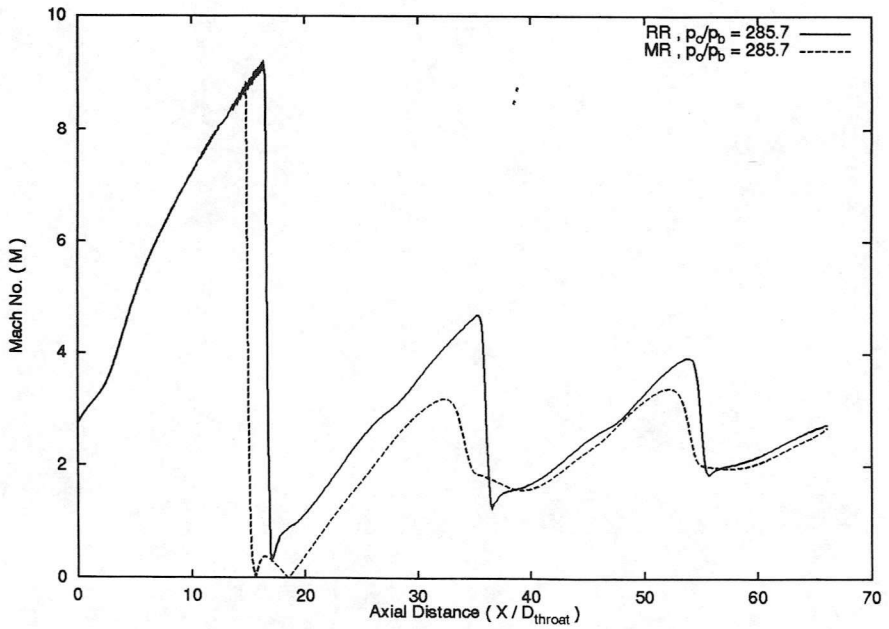

Figure 4.32: *Centre-line Mach no. comparison, regular and Mach reflection*

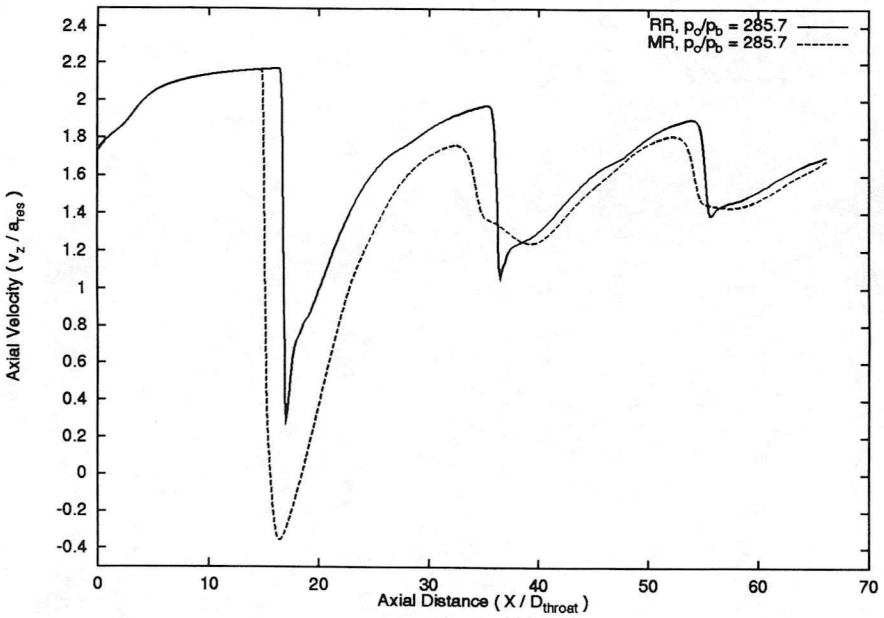

Figure 4.33: *Centre-line axial velocity comparison, regular and Mach reflection*

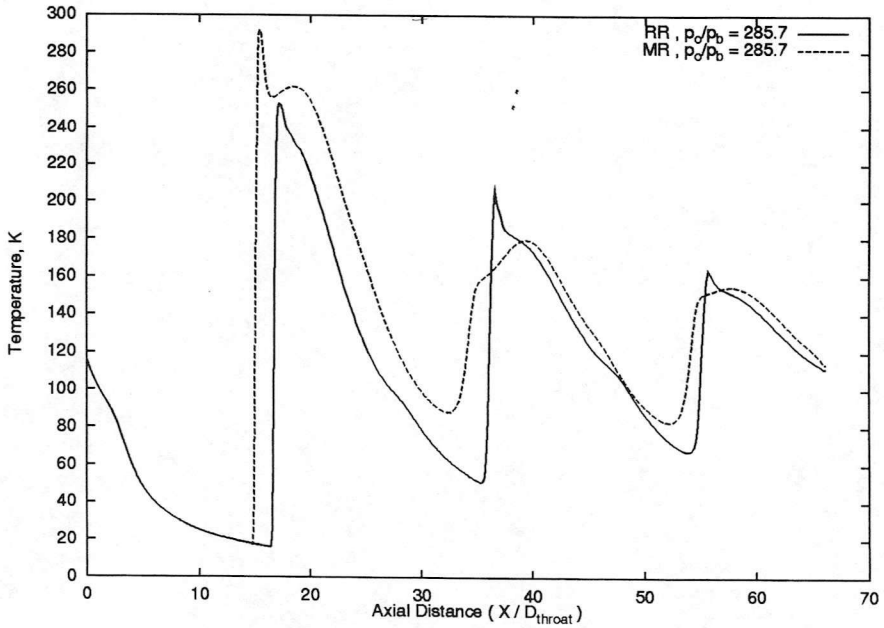

Figure 4.34: *Centre-line temperature comparison, regular and Mach reflection* T_o = *288.0 K*

4.4 Discussion

A hysteresis effect has been predicted in the shock reflection type of an axisymmetric jet plume for a range of pressure ratios and a constant Reynolds number. The predicted hysteresis loop agrees well with experimental results where the Reynolds number was also varying. Uncertainty whether a regular reflection or a Mach reflection with a small diameter Mach disc is being predicted in one half of the hysteresis loop does not detract from the main conclusion that a hysteresis phenomenon concerning two reflection types has been captured. Suggestions have been made for future work to eliminate this uncertainty. The influence of viscosity on the reflection type could be examined in a similar manner to the present study by performing the same calculations for a range of Reynolds number. A study of the shock reflection hysteresis in isolation rather than in the context of a jet plume would be much simpler to perform and could lead to a clearer understanding of the mechanisms involved, without the complications of curved shocks, shear layers etc. An analysis of the present computational results using the methods used for the problem of two dimensional shock reflection hysteresis in uniform flow would require more accurate shock wave resolution than achieved in the present study.

The value of a CFD analysis has been clearly demonstrated by the detail that can be obtained from the results. The recirculation region and continuing compression behind the Mach disc are features not recognised in the original experimental study, which may be re-examined in future tests. This is an example of the progress possible when CFD and experiments are exploited in a complementary fashion.

The computational results presented here have not been compared in detail with experimental data. This data should become available in the near future and such

a comparison will be made. However, comparison "by eye" of the present results and the plotted shock reflection distance and centre-line results in [2] has given the authors some confidence in the validity of the calculations.

Chapter 5

Conclusion

The hysteresis effect in underexpanded jet plumes reported by Welsh [2] has been successfully predicted using a CFD approach. The results agree well qualitatively with experiment. Some quantitative comparison has been possible, showing reasonable agreement. More detailed comparison will be made with experimental data when it becomes available. The scatter present in the experimental results and possible sources of discrepency between computational and experimental results were explained. The detailed CFD results identified some flow features not recognised in experiments. Some suggestions are made for further CFD examination of this problem. Included in this study is a review of two-dimensional shock reflection hysteresis which has highlighted some remaining gaps in the understanding of this phenomenon. An attempt has been made to fill these gaps by applying the principle of minimum entropy production.

Bibliography

[1] C. Crist, P.M. Sherman and D.R. Glass. Study of the Highly Underexpanded Sonic Jet. *AIAA Journal*, 4(1):68–71, 1966.

[2] F.P. Welsh. Shock Reflection Hysteresis in Low Density Under-Expanded Jets. *DRA Technical Report DRA/DWS/WX9/CR97361*, March 1997.

[3] P. Reijasse, B. Corbel and J. Delery. Flow Confluence Past a Jet-On Axisymmetric Afterbody. *Journal of Spacecraft and Rockets*, 34(5):593–601, Sep-Oct 1997.

[4] S.M. Prudhomme, and H. Haj-Hariri. Investigation of Supersonic Underexpanded Jets using Adaptive Unstructured Finite Elements. *Finite Elements in Analysis and Design*, 17:21–40, 1994.

[5] P.S. Cumber, M. Fairweather, S.A.E.G. Falle and J.R. Giddings. Predictions of the Structure of Turbulent, Highly Underexpanded Jets. *Journal of Fluids Engineering*, 117:599–604, Dec 1995.

[6] V. Salemann and J.M. Williams. New Method of Modelling Underexpanded Exhaust Plumes for Wind Tunnel Aerodynamics Testing. *Journal of Engineering for Gas Turbines and Power*, 111(4):748–754, Oct 1989.

[7] C. Dankert, R.D. Boettcher, G. Detteleff and H. Legge. Plume Size Measurements on Underexpanded Jets in Vacuum Chambers. *AIAA-85-0932*, Oct 1985.

[8] T.F. Hu and D.K. McLaughlin. Flow and Acoustic Properties of Low Reynolds Number Underexpanded Supersonic Jets. *Journal of Sound and Vibration*, 141(3):485–505, Sept 1990.

[9] V.V. Riabov. Aerodynamic Applications of Underexpanded Viscous Jets. *Journal of Aircraft*, 32(3):471–479, May-June 1995.

[10] M. Abbett. Mach Disk in Underexpanded Exhaust Plumes. *AIAA Journal*, 9(3):512–514, March 1971.

[11] J.H. Fox. On the Structure of Jet Plumes. *AIAA Journal*, 12(1):105–107, 1974.

[12] I.S. Chang and W.L. Chow. Mach Disk from Underexpanded Axisymmetric Nozzle Flow. *AIAA Journal*, 12(8):1079–1082, 1974.

[13] D.W. Eastman and L.P. Radtke. Location of the Normal Shock Wave on the Exhaust Plume of a Jet. *AIAA Journal*, 1(4):918–919, 1963.

[14] A.T. Hsu and M.S. Liou. Computational Analysis of Underexpanded Jets in the Hypersonic Regime. *Journal of Propulsion and Power*, 7(2):297–299, 1991.

[15] P. Birkby, J.C. Dent and G.J. Page. CFD prediction of Turbulent Sonic Underexpanded Jets. In *Proceedings of the 1996 ASME Fluids Engineering Summer Meeting. Part 2 (of 3)*, pages 465–470, Jul 7-11 1996.

[16] H.G. Hornung, H. Oertel Jnr. and R.J. Sandeman. Transition from Mach Reflection of Shock Waves in Steady and Pseudosteady Flow With and Without Relaxation. *Journal of Fluid Mechanics*, 90:541–560, 1979.

[17] A. Chpoun, D. Passerel, H. Li and G. Ben-Dor. Reconsideration of Oblique Shock Wave Reflection in Steady Flows. Part I: Experimental Investigation. *Journal of Fluid Mechanics*, 301:19–35, 1995.

[18] J. Vuillon, D. Zeitoun and G. Ben-Dor. Reconsideration of Oblique Shock Wave Reflection in Steady Flows. Part II: Numerical Investigation. *Journal of Fluid Mechanics*, 301:37–50, 1995.

[19] M.S. Ivanov, S.F. Gimelshein and A.E. Beylich. Hysteresis Effect in Stationary Reflection of Shock Waves. *Physics of Fluids*, 7(4):685–687, 1995.

[20] M.S. Ivanov, D. Zeitoun, J. Vuillon, S.F. Gimelshein and G. Markelov. Investigation of the Hysteresis Phenomena in Steady Shock Reflection Using Kinetic and Continuum Methods. *Shock Waves*, 5(6):341–346, 1996.

[21] H.G. Hornung. Regular and Mach Reflection of Shock Waves. *Annual Reveiw of Fluid Mechanics*, 18:33–58, 1986.

[22] G. Ben-Dor. Steady, Pseudo-Steady and Unsteady Shock Wave Reflections. *Progress in Aerospace Sciences*, 25:329–412, 1988.

[23] H.G. Hornung and M.L. Robinson. Transition from regular to Mach Reflection of shock waves Part 2 . The steady-flow criterion. *Journal of Fluid Mechanics*, 123:155–164, 1982.

[24] H. Li and G. Ben-Dor. Application of the Principle of Minimum Entropy Production to Shock Wave Reflections. I. Steady Flows. *Journal of Applied Physics*, 80(4):2027–2037, 1996.

[25] L.F. Henderson and A. Lozzi. Further Experiments on Transition to Mach Reflection. *Journal of Fluid Mechanics*, 94(3):541–559, 1979.

[26] Ames Research Staff. Equations, Tables and Charts for Compressible Flow. *NACA Report 1135*, 1953.

[27] D.J. Azedevo and C.S. Liu. Engineering Approach to the Prediction of Shock Patterns in Bounded High-Speed Flows. *AIAA Journal*, 31(1):83–90, 1993.

[28] L.F. Henderson and A. Lozzi. Experiments on Transition of Mach Reflection. *Journal of Fluid Mechanics*, 68(1):139–155, 1975.

[29] G. Ben-Dor, T. Elperin and E. Golshtein. Monte Carlo Analysis of the Hysteresis Phenomenon in Steady Shock Wave Reflections. *AIAA Journal*, 35(11):1777–1779, 1997.

[30] P. Glansdorff and I. Prigogine. *Thermodynamic Theory of Structure, Stability and Fluctuations.* Wiley-Interscience, U.K., 1971.

[31] M.D. Salas and B.D. Morgan. Stability of Shock Waves Attached to Wedges and Cones. *AIAA Journal*, 21(12):1611–1617, 1983.

[32] H. Li and G. Ben-Dor. Application of the Principle of Minimum Entropy Production to Shock Wave Reflections. I. Pseudosteady Flows. *Journal of Applied Physics*, 80(4):2038–2048, 1996.

[33] R.E. Balzhiser, M.R. Samuels and J.D. Eliassen. *Chemical Engineering Thermodynamics.* Prentice-Hall, U.S.A., 1972.

[34] K.J. Badcock, W. McMillan, M.A. Woodgate, B.J. Gribben, S. Porter and B.E. Richards. Integration of an Implicit Multiblock Code into a Workstation Cluster Environment. In P. Schiano et al., editor, *Parallel Computational Fluid Dynamics: Algorithms and Results using Advanced Computers*, pages 408–415. Elsevier Science B.V. Amsterdam, 1996.

[35] F. Cantariti, L. Dubuc, B.J. Gribben, M. Woodgate, K.J. Badcock and B.E. Richards. Approximate Jacobians for the Euler and Navier-Stokes Equations. *University of Glasgow, Aero Report 9705*, 1997.

[36] B.J. Gribben, K.J. Badcock and B.E. Richards. Application of PMB2D to Axisymmetric Flows. *University of Glasgow, Aero Report 98??*, 1998.

[37] W.G. Vincenti and C.H. Kruger Jr. *Introduction to Physical Gas Dynamics.* John Wiley & Sons, U.S.A., 1965.

[38] S. Chapman and T.G. Cowling. *The Mathematical Theory of Non-Uniform Gases.* Cambridge University Press, U.K., 1960.

[39] J. D. Anderson Jr. *Hypersonic and High Temperature Gas Dynamics.* McGraw-Hill Book Company, U.S.A., 1989.

[40] F.L. Daum and G. Gyarmathy. Condensation of Air and Nitrogen in Hypersonic Wind Tunnels. *AIAA Journal*, 6(3):458–465, 1968.